

We would like to thank the reviewer 1 for their helpful comments that improved this manuscript. Below in *italics* please, find our replies to the reviewer's comments. Following their comments, we have revised the manuscript as outlined below: (1) We have added two new figures (and related discussion) comparing the two versions over source regions and highly polluted cities; (2) We have addressed all comments raised by the reviewer.

I have three major concerns with this manuscript:

1. While this document would make a very good ATBD for the new OMI product, it is not a very good paper in my opinion. The reason is that most of what is described in section 2 is a summary of what the authors have already published elsewhere, and while it is good to summarize everything in one place for data users, I did not see anything new here. If I missed something and the algorithms as now implemented in the OMI processor deviate from what was published in Vasilkov et al., 2017, Vasilkov et al., 2018 and Qin et al., 2019, then this should be highlighted.

We disagree with those characterizations regarding this manuscript. This is the first version of the OMI NO₂ Standard Product (OMNO2) with global implementation, extensive evaluation, and mission-long processing utilizing 1) a new concept of geometry-dependent surface reflectivity product (GLER) as introduced in Vasilkov et al. (2017); 2) new cloud product first introduced in Vasilkov et al (2018); 3) surface reflectivity product over land discussed in Qin et al (2019) and over water in Fasnacht et al (2019). The first two manuscripts presented conceptual demonstrations and case studies, and the latter two manuscripts provided detailed descriptions and validation of the GLER product at 466 nm. This work, while building on our prior works, expands them to the NO₂ spectral window (centered at 440 nm) as described in the manuscript. In this manuscript, our intension was to initially provide a brief summary of the relevant new developments in a single document as pointed out by the reviewer and then elaborate on additional new implementations that are relevant for NO₂ retrievals. The NO₂ relevant implementations are discussed on pages 10-11 for GLER, pages 13-14 for cloud parameters, and pages 14-15 for treatment over ice/snow surfaces.

2. What data users need to know is how the product changed relative to the last version. Some nice analysis is done on this as shown in Figs. 3 – 6, and I found this very interesting. However, this is only based on one day of data and does not differentiate by region, and I actually took a wrong message from this analysis, namely to expect a very significant (20 – 40 %) and consistent increase in tropospheric NO₂ columns, in particular for large NO₂ columns. However, as can be seen from Figure 12, this is not universally true, the differences for all Pandora stations been much smaller than what is expected from Figure 6! This is also evident from Fig. 11, where the version differences for Greenbelt have a clear seasonality. I think that the authors should pick a couple of regions representative for different NO₂ scenarios (polluted places, very polluted places, biomass burning regions, soil emission regions, lightning regions) and present differences between the two data versions as a function of season as done for Greenbelt in Fig. 11. This would give the reader a much better idea of which changes to expect where and when, and such an analysis should be relatively simple to do. It would also be nice to see an example of BRDF effects on the NO₂ columns outside of sun glint regions – this is a major improvement of the new data version and it would be interesting to see if it has a noticeable effect on the tropospheric NO₂ columns.

This is indeed an excellent suggestion. We have included 2 additional figures (Figures 11 and 12) comparing V3.1 and V4.0 over source regions, and over highly polluted cities. We have expanded Section 2.5 discussing the impact of the changes as follows:

“Figure 11 shows some examples of how changes in the algorithm from V3.1 to V4.0 affect monthly average tropospheric NO₂ columns over areas affected by various NO_x sources. In contrast to minor changes over the pristine Pacific Ocean, month-to-month changes over source regions vary considerably. The differences in tropospheric NO₂ columns between V4.0 and V3.1 range from -11 to 15% over Beijing, China and from 0 to 29% over the Ruhr area in Germany, suggesting variations in relative differences among cities and industrial areas. The changes over a major biomass burning area of Democratic Republic of Congo, Angola, and Zambia range 13-56% during the biomass burning season of May through August, but are <5% in other months. Differences between the two versions are small over areas influenced by lightning NO_x emissions. In Figure 12, we examine monthly variation of tropospheric NO₂ columns from the two versions over five highly populated and polluted cities that vary in terrain types ranging from coastal (e. g., Shanghai, Tokyo) to mountainous (e.g., Mexico City). NO₂ columns in V4.0 are generally higher than V3.1 by 0-30%, but the difference can occasionally reach up to 50% in some months. Changes of that order of magnitude in highly polluted areas have implications for estimation of NO_x emissions and trends using these data.”

3. The authors call this OMI NO₂ data version “improved”, and I tend to agree that the GLER surface treatment is an improvement over the use of a static reflectivity database not covering angular effects. However, the validation data shown is inconclusive, and to me it looks as if any changes in the product are within the combined uncertainties of retrievals, validation measurements and representation errors. Based on these results, there is little reason to move to the new data version! It would therefore really be nice if the authors could find an example of where the new NO₂ product performs clearly better than the last version.

The validation data sets for NO₂ are scarce and are limited in space and time. In addition, validation data have their own issues, such as representativeness error and retrieval issues with Pandora observations and lack of measurements in the lowest few hundred meters in case of aircraft spiral measurements. Therefore, validation of the global product as presented in this manuscript is limited in scope by spatial and temporal coverage and retrieval conditions, and obviously are not representative of other locations and seasons. This is evident from the wide range of variation in results presented in Figures 8-11. We believe that the new results presented in Figures 11 and 12 as suggested by the reviewer have helped address the concerns.

1. Add product version number to title

*We have included version number in the title. The title now reads as “**OMI/Aura Nitrogen Dioxide Standard Product Version 4.0 with Improved Surface and Cloud Treatments**”*

2. line 21: Not sure what the authors refer to by “regional” here – as far as I can see, the improvements presented here are for the global product while the most important improvement for regional products (high resolution a priori NO₂ profiles) has not been addressed. I would suggest rephrasing.

Removed “regional” and “on a global scale” from the statement. It now reads as “This version incorporates the most salient improvements for OMI NO₂ products suggested by expert users and

enhances the NO₂ data quality in several ways through improvements to the air mass factors (AMFs) used in the retrieval algorithm.”

3. line 24: While the GLER was conceptually new when proposed by Vasilkov et al., 2017, it is not in this manuscript. I would suggest rephrasing.

Removed “a conceptually new,” from the statement. It now reads as “The algorithm is based on geometry-dependent surface Lambertian equivalent reflectivity (GLER) operational product that is available on an OMI pixel basis.”

4. line 31 / 32: I would hope that all inputs to the AMF scheme are of high quality! I also don't think that a “new NO₂ AMF scheme” is presented just because the AMF module reads other inputs. I would suggest rephrasing.

Modified the statement as “The GLER combined with consistently retrieved oxygen dimer (O₂-O₂) absorption-based effective cloud fraction (ECF) and optical centroid pressure (OCP) provide improved information to the new NO₂ AMF calculations”

5. line 36 / 37: Nothing is said in the manuscript on emission and trend analysis of NO_x, let alone of other trace gases. I therefore suggest removing this sentence.

Removed.

6. line 43 – 45: I think this sentence fits better to an outreach leaflet than to a scientific paper.

The statement is modified as “The Dutch/Finnish-built Ozone Monitoring Instrument (OMI) has been operating on board the NASA EOS-Aura spacecraft since July 2004 (Levelt et al., 2006, 2018)”

7. line 71: bseen => been

Corrected.

8. line 92: “day-to-day (orbital) variability in surface reflectance“ – I find this formulation confusing as in my view, it is not the surface reflectance which is changing from day to day but the viewing geometry which leads to a variation in reflectance at TOA.

Bidirectional Reflection Distribution Function (BRDF) is an inherent property of any surface, but apparent surface reflectance, not just top of atmosphere (TOA) radiance, does depend on sun-view geometry. The statement is correct. However, we modified the statement as follows: “In addition, the OMLER approach neglects significant variabilities inherent of surface bidirectional reflectance resulting from day-to-day (orbital) variation in sun-satellite angles.”

62: What was done for SZA > 70 where use of MCD43GF is not recommended?

Thank you for pointing out the data quality issue in the MCD43 product for SZA > 70. In the MCD43GF product, data at high SZA areas are interpolated linearly using retrievals over the same geographical area observed at lower SZAs. Therefore, these data are expected to be of inferior quality, and cautious interpretation is needed. We have clarified this in the revised manuscript.

469: is => are

Done.

474: is => are

Done.

69: delete “retrieved”

Done.

16: Differences in vertical sensitivity – isn’t that already corrected for by the AMF?

Sorry for the confusion. This refers to the difference in vertical sensitivity between satellite and ground-based observations as stated in the manuscript. The vertical sensitivity is accounted for through scattering weights and assumed profile shapes used in the AMF calculations for OMI, but Pandora uses a type of geometric correction as discussed in Herman et al. (2009). The difference in approach is still relevant for the observed difference between OMI and Pandora retrievals.

68: “to relatively OMI’s large pixels” => “to OMI’s relatively large pixels”

Done.

Figure 1: What are the Ps coming from the GLER module?

Ps represents calculated surface pressure over OMI pixel. This is clarified in Figure 1.

We would like to thank the reviewer 2 for their helpful comments that improved this manuscript. Below in *italics* please, find our replies to the reviewer's comments. We have revised our manuscript by adding two new figures (and related discussion) comparing the two versions over source regions and highly polluted cities, and addressing all other comments raised by the reviewer.

=====

The authors present a new version of NASA's standard OMI NO₂ algorithm, which includes several improvements: better surface reflectance treatment, new cloud product based on the updated surface reflectance, and several other improvements. The effects on AMFs are shown for global maps for specific days. The effects on VCDs are shown for specific days and long-term average. The new product has been evaluated with ground-based and airborne observations. The manuscript is generally well written and the new product version fits well within the scope of the AMT. I recommend publication of the manuscript after considering the comments below:

(1) The analysis of the AMFs focus on some daily global maps. The largest difference between V3.1 and V4.0 should be actually noticeable at the regional and local scale as also discussed in the manuscript. I suggest to add some example figures that show the improvement at that scale, for example, along polluted coastlines, in the presence of snow, or in mountainous terrain. These figures would also be important to demonstrate the new version is actually superior to the previous version.

We agree that additional figures could help show the extent of changes between V3.1 and V4.0. Our global and regional maps already show changes over coastlines, snow, and mountains. Following the suggestions from both reviewers, we decided to include additional examples from source regions as well as five highly populated cities that can represent different geographic terrain (e.g., polluted coastal city). We have expanded Section 2.5 discussing the impact of the changes as follows:

"Figure 11 shows some examples of how changes in the algorithm from V3.1 to V4.0 affect monthly domain average tropospheric NO₂ columns over areas affected by various NO_x sources. In contrast to minor changes over the pristine Pacific Ocean, month-to-month changes over source regions vary considerably. The differences in tropospheric NO₂ columns between V4.0 and V3.1 range from -11 to 15% over Beijing, China and from 0 to 29% over the Ruhr area in Germany, suggesting variations in relative difference among cities and industrial areas. The changes over a major biomass burning area of Democratic Republic of Congo, Angola, and Zambia range 13-56% during the biomass burning season of May through August, but are <5% in other months. Differences between the two versions are small over areas influenced by lightning NO_x emissions. In Figure 12, we examine monthly variation of tropospheric NO₂ columns from the two versions over five highly populated and polluted cities that vary in terrain types ranging from coastal (e.g., Shanghai, Tokyo) to mountainous (e.g., Mexico City). NO₂ columns in V4.0 are generally higher than V3.1 by 0-30%, but the difference can occasionally reach up to 50% in some months. Changes of that order of magnitude in highly polluted areas have implications for estimation of NO_x emissions and trends using these data."

(2) The evaluation of the new product is quite short and could be extended with some additional analysis. In particular, it is currently difficult to judge if the new version significantly improves the product, because the authors do not evaluate both V3.1 and V4.0 for all data. It would also be

helpful to have table with correlation coefficient, bias and other parameters to give an overview over these numbers currently spread throughout the manuscript.

This is indeed a good suggestion. Some of the validation results shown here for V4.0 are extension of our previous study with V3.1 discussed in detail in Choi et al (2020), which we have cited in several places of this manuscript. Therefore, we chose not to include them for V3.1. We have added a summary table (Table 2) for the validation results as suggested by the reviewer.

L55ff: The row anomaly is only mentioned in Section 2.4 but I would consider already briefly mention it at the beginning of Section 2 because the impact on data availability is unfortunately quite severe.

We have added the following statement in Section 2 “OMI’s full daily coverage has been affected by data loss due to an anomaly presumably caused by material on the spacecraft outside the instrument that results in reduced coverage to about half of its original swath as discussed in Section 2.4.”

L99: MODIS surface reflectance has also been used in the HKOMI product (Kuhlmann et al. 2015, <https://doi.org/10.5194/acp-15-5627-2015>).

Thanks. The new reference is added on Page 4, line 115.

L435: Please mention somewhere that "coastal areas" refers to the high NO₂ values labelled with "ocean" in Figure 6.

This is clarified as suggested. We now state “cities and highly polluted coastal areas”.

L441ff: The term "lower troposphere" is somewhat confusing here, because it should be the additional layers between the new and old cloud pressure and not the full lower troposphere.

We agree; the statement now reads as: “Higher values of OCP in OMCD02N will include additional portions of scattering weights between the OMCD02N- and OMCLD02-based OCPs, especially in the lower troposphere, thereby reducing the tropospheric AMF.”

L444f: ". . .in the calculation of tropospheric AMF." -> ". . .in the calculation of tropospheric AMF increasing the AMF."

The statement is modified as suggested “On the other hand, the higher CRF values lead to an increased contribution of the cloudy AMF in the calculation of tropospheric AMF, thereby increasing its value.”

L459ff: What is the reason for the increase of AMFs over ocean in Fig. 5c?

The apparent change in tropospheric AMFs over ocean in Figure 5c due partly to changes in terrain pressure and partly to color bar issue. The changes are small at about 1%. The relevant statement is modified on Page 17, Line 477.

L528: Please add a sentence that explains what kind of improvement is expected when improved NO₂ profiles become available.

The statement is modified to include possible approaches for improving a priori NO₂ profiles as follows: “Further improvement to the retrievals is possible by enhancing the quality of a priori NO₂ profiles through improvements in model resolution, emissions, and chemistry, which remain unchanged in the current version.”

L532f: The effect of the a priori is not really removed "altogether" when NO₂ profiles are used for model comparison but remains as part of the model error.

Indeed, the use of model-derived inputs affects retrievals. The context here though is different, and is related to an issue that is often raised while comparing simulated NO₂ with retrievals. Eskes and Boersma (2003) discuss an approach of using averaging kernel to remove the effect of a priori NO₂ profiles used in retrievals while comparing model-derived NO₂ columns with retrievals. An alternative approach of using scattering weights for the same purpose is discussed in Lamsal et al (2014). We have added these references to clarify the context.

L676: What do you mean by the "alternating nature of the variation"? Please provide more details. *We realize that the statement was not clear. The statement is now revised as follows: "This alternating nature of the variation in results in polluted versus clean areas suggests that OMI's large footprint size and narrow spiral radius (~4 km) of the aircraft are likely the primary cause for the observed differences. This was demonstrated in Choi et al. (2020) by using high-resolution Community Multi-scale Air Quality Model (CMAQ) simulations."*

L684: Please specify how the "agreement" was computed here and which parameter has improved by 20-35

The statement is modified in the revised version for clarity as follows: "The use of observed profiles in the OMI retrievals leads to a slight change in correlation, but 20-35% reduction in mean difference between OMI and aircraft observations, highlighting the role of a priori profiles in NO₂ retrievals as suggested by previous studies (Russell et al., 2011; Lamsal et al., 2014; Goldberg et al., 2017; Laughner et al., 2019; Choi et al., 2020)."

L725ff: The sentence is a bit confusing. Does the 0.3 refers to the GLER or to the difference between GLER and LER?

This value of 0.3 refers to GLER. The statement is correct, but is modified for clarity as follows: "The data from GLER (a unitless value with 0.0-1.0 range) are generally lower, by <0.05, than the climatological LER data over land and ocean outside of sunglint areas; GLER is much higher over the sunglint areas that reaches more than 0.3 due to the geometry-dependent Fresnel reflection."

L726 L732: The formulation "lower by "the optimized"?

It should have been "lower than V3.1". It is corrected.

L742: "may" -> "can"

Done.

Figure 1 lists many abbreviations used in the paper. It would be better to list them in a table instead of the caption of a figure.

Those abbreviations are already defined in the text. Re-defining them in the figure caption helps readers understand various terminologies and acronyms without switching back and forth between other texts or table and this figure.

1 **OMI/Aura Nitrogen Dioxide Standard Product [Version 4.0](#) with Improved Surface**
2 **and Cloud Treatments**

3
4
5 Lok N. Lamsal ^{*,1,2}, Nickolay A. Krotkov², Alexander Vasilkov^{2,3}, Sergey Marchenko^{2,3},
6 Wenhan Qin^{2,3}, Eun-Su Yang^{2,3}, Zachary Fasnacht^{2,3}, Joanna Joiner², Sungyeon Choi^{2,3}, David
7 Haffner^{2,3}, William H. Swartz⁴, Bradford Fisher^{2,3}, Eric Bucsela⁵

8
9 ¹University Space Research Association, Greenbelt, MD 20770, USA

10 ²NASA Goddard Space Flight Center, Greenbelt, MD 20770, USA

11 ³Science Systems and Applications, Lanham, MD 20706, USA

12 ⁴Johns Hopkins University, Applied Physics Laboratory, Laurel, MD 20723, USA

13 ⁵SRI International, Menlo Park, CA 94025, USA

14
15
16
17 *Corresponding author: Email: lok.lamsal@nasa.gov.

18 **Abstract**

19 We present a new and improved version (V4.0) of the NASA standard nitrogen dioxide (NO₂)
20 product from the Ozone Monitoring Instrument (OMI) on the Aura satellite. This version
21 incorporates the most salient improvements for OMI NO₂ products suggested by expert users and
22 enhances the NO₂ data quality in several ways through improvements to the air mass factors
23 (AMFs) used in the retrieval algorithm. The algorithm is based on geometry-dependent surface
24 Lambertian equivalent reflectivity (GLER) operational product that is available on an OMI pixel
25 basis. GLER is calculated using the vector linearized discrete ordinate radiative transfer
26 (VLIDORT) model, which uses as input high resolution bidirectional reflectance distribution
27 function (BRDF) information from NASA's Aqua Moderate Resolution Imaging
28 Spectroradiometer (MODIS) instruments over land and the wind-dependent Cox-Munk wave-
29 facet slope distribution over water, the latter with contribution from the water-leaving radiance.
30 The GLER combined with consistently retrieved oxygen dimer (O₂-O₂) absorption-based effective
31 cloud fraction (ECF), and optical centroid pressure (OCP), provide improved information to the
32 new NO₂ AMF calculations. The new AMFs increase the retrieved tropospheric NO₂ by up to 50%
33 in highly polluted areas; these differences arise from both cloud and surface BRDF effects as well
34 as biases between the new MODIS-based and previously used OMI-based climatological surface
35 reflectance data sets. We quantitatively evaluate the new NO₂ product using independent
36 observations from ground-based and airborne instruments. The new V4.0 data and relevant
37 explanatory documentation are publicly available from the NASA Goddard Earth Sciences Data
38 and Information Services Center (https://disc.gsfc.nasa.gov/datasets/OMNO2_V003/summary/),
39 and we encourage their use over previous versions of OMI NO₂ products.

Deleted: regional

Deleted: ,

Deleted: on a global scale

Deleted: a conceptually new,

Deleted: s

Deleted: s

Deleted: high-quality data inputs

Deleted: scheme

Deleted: The improved NO₂ data record can be used for studies related to emissions and trends of nitrogen oxides (NO_x) and co-emitted gases.

51 Introduction

52 The Dutch/Finnish-built Ozone Monitoring Instrument (OMI) [has been operating on board the](#)
53 NASA EOS-Aura [spacecraft since July 2004](#) (Levelt et al., 2006, 2018). The primary objectives
54 of OMI's mission are to continue the long-term record of total column ozone and to monitor other
55 trace gases relevant to tropospheric pollution worldwide. Observations of sunlight backscattered
56 from the Earth over a wide range of UV and visible wavelengths (~260-500 nm) made by OMI
57 allow for the retrieval of various atmospheric trace gases, including nitrogen dioxide (NO₂). NO₂
58 is a critically important short-lived air pollutant originating from both anthropogenic and natural
59 sources. It is the principal precursor to tropospheric ozone and a key agent for the formation of
60 several toxic airborne substances such as nitric acid (HNO₃), nitrate aerosols, and peroxyacetyl
61 nitrate. Satellite-based observations yield a global, self-consistent NO₂ data record that can
62 complement field measurements.

63 During more than [16 years of operation](#), OMI has provided a unique, practically uninterrupted
64 daily NO₂ data record that has been widely used for atmospheric research and applications,
65 accentuating demands for accurate NO₂ data products. The power of OMI to track NO₂ pollution
66 is demonstrated through observations of enhanced column amounts over polluted industrial areas
67 (*e.g.*, Boersma et al., 2011; Lamsal et al., 2013; Krotkov et al., 2016; Kim et al., 2016; Cai et al.,
68 2018; Montgomery and Halloway, 2018), weekly patterns with significant reduction on weekends
69 following energy usage (*e.g.*, Ialongo et al., 2016), and seasonal patterns (*e.g.*, van der A et al.,
70 2008) that reflect changes in NO_x emissions and photochemistry (*e.g.*, Shah et al., 2019).
71 Exploiting the close relationship between NO_x emissions and tropospheric NO₂ columns, OMI
72 NO₂ data have been used to detect and quantify the strength and trends of NO_x emissions from
73 power plants (Duncan et al., 2013; de Foy *et al.*, 2015; Liu et al., 2019), ships (*e.g.*, Vinken et al.,
74 2014a), lightning (*e.g.*, Picketing et al., 2016), soil (*e.g.*, Vinken et al., 2014b), oil and gas
75 production (*e.g.*, Dix et al., 2020), forest fires (Schreier et al., 2014), and other area sources such
76 as cities in the US (Lamsal *et al.*, 2015; Lu *et al.*, 2015; Kim et al., 2016), Europe (*e.g.*, Zhou et
77 al., 2012; Castellanos et al., 2012; Vinken et al., 14a), Asia (Ghude et al., 2013; Goldberg et al.,
78 2019a), and other world urban areas (Krotkov *et al.*, 2016; Duncan *et al.*, 2016; Montgomery and
79 Halloway, 2018). OMI NO₂ observations have frequently [seen used to evaluate chemical transport](#)
80 models (CTMs) (*e.g.*, Herron-Thrope et al., 2010; Han et al., 2011; Hudman et al., 2012; Pope et
81 al., 2015; Rasool et al., 2016), to study atmospheric NO_x chemistry and lifetime (*e.g.*, Lamsal et

Deleted: satellite and its international science team are part of a successful multi-institutional, multi-national collaborative program in the measurement of atmospheric composition ...

Deleted: 5

Deleted: b

88 al., 2010; Beirle et al., 2011; Canty et al., 2015; Tang et al., 2015; Laughner and Cohen, 2019),
89 and to infer ground-level NO₂ concentrations (Lamsal et al., 2008; Gu et al., 2017), NO₂ dry
90 deposition (Nowlan et al., 2014, Geddes and Martin, 2017), and emissions of co-emitted gases
91 including carbon dioxide (CO₂) (Konovalov et al., 2016; Goldberg et al., 2019b, Liu et al., 2019).

92 Over the last decade, there have been considerable efforts to improve NO₂ data quality from OMI
93 and other satellite instruments (e.g., Boersma et al., 2018). A special emphasis has been placed on
94 improving auxiliary information (e.g., a priori NO₂ vertical profiles, surface reflectivity),
95 particularly with respect to spatial and temporal resolution. For instance, the global OMI NO₂
96 products are based on a priori NO₂ profiles from relatively coarse-resolution (>1.0°× 1.25°) global
97 CTM simulations (Boersma et al., 2011; Krotkov et al., 2017, Choi et al., 2020). Many regional
98 studies suggest a general low-bias in the global tropospheric NO₂ column products, particularly
99 over polluted areas, that can be partially mitigated by using a-priori information from high-
100 resolution CTM simulations (Russell et al., 2011, McLinden et al., 2014; Lin et al., 2014; 2015;
101 Goldberg et al., 2018; Choi et al., 2020). Current global NO₂ retrievals are based on a low-
102 resolution (0.5°× 0.5°) static climatology of surface Lambert-Equivalent Reflectivity (OMLER)
103 product (Kleipool et al., 2008), which is likely biased high due to insufficient cloud and aerosol
104 screening. This bias in surface reflectivity can lead to an underestimation of tropospheric NO₂
105 retrievals (Zhou et al., 2010; Lin et al., 2014; Vasilkov et al., 2017). In addition, the OMLER data
106 do not account for the significant day-to-day (orbital) variability in surface reflectance caused by
107 changes in sun-satellite geometry, a phenomenon often expressed by the bi-directional reflectance
108 distribution function (BRDF). Zhou et al. (2010) demonstrated the impact of both the spatial
109 resolution and the BRDF effect on OMI tropospheric NO₂ retrievals over Europe by using high-
110 resolution surface BRDF and albedo products from the Moderate Resolution Imaging
111 Spectroradiometer (MODIS). Taking advantage of the MODIS high resolution data, albeit
112 neglecting the BRDF and atmospheric effects, Russell et al (2011) and McLinden et al (2014)
113 created improved NO₂ products from the NASA Standard Product (Bucsela et al., 2013; Lamsal
114 et al., 2014) over the continental US and Canada, respectively. While these and subsequent studies
115 (e.g., [Kuhlmann et al., 2015](#); Laughner et al., 2019) addressed the limitation of climatological LER
116 data on NO₂ retrievals, they did not account for the surface BRDF effect on the OMI cloud products
117 (cloud pressure/fraction), which are also inputs to the NO₂ algorithm. Applying the MODIS BRDF
118 data consistently to both the NO₂ and cloud retrievals demonstrably improves the quality of OMI

119 NO₂ retrievals over China (Lin et al., 2014, 2015, Liu et al., 2019). However, this approach is
120 computationally expensive and is applicable to land surfaces only. Our previous work (Vasilkov
121 et al., 2018) proposed an approach appropriate for satellite NO₂ data processing on a global scale
122 (a) by using MODIS BRDF information consistently in the cloud and NO₂ retrievals; (b) for both
123 land and water; and (c) in an efficient way. Here, we apply the approach globally for the first time
124 in the standard NASA OMI NO₂ algorithm.

125 In this paper we describe various updates made in the version 4.0 (V4.0) NASA OMI NO₂
126 algorithm, discuss their impact on the retrievals of tropospheric and stratospheric NO₂ column
127 amounts, and provide an initial quantitative assessment of NO₂ data quality. Section 2 describes
128 the OMI NO₂ algorithm and various auxiliary data used by the algorithm. We present validation
129 results in Section 3. Section 4 summarizes the conclusions of this study.

130 **2 OMI and the NO₂ Standard Product**

131 OMI is a ultraviolet-visible (UV-Vis) spectrometer on the polar-orbiting NASA Aura satellite
132 (Levelt et al., 2006, 2018). Aura, launched on July 15, 2004, follows a sun-synchronous orbit with
133 an equator crossing time near 13:45 local time. OMI employs two-dimensional CCD detectors and
134 operates in a push-broom mode, registering spectral data over a 2600 km cross-track spatial swath.
135 The broad swath enables global daily coverage within 14-15 orbits. In the OMI visible channel
136 used for NO₂ retrievals, each swath, measured every two seconds, comprises 60 cross-track fields
137 of view (FOVs) varying in size from ~13 km × 24 km near nadir to ~24 km × 160 km for the FOVs
138 at the outermost edges of the swath. Each orbit consists of ~1650 swaths from terminator to
139 terminator. [OMI's full daily coverage has been affected by data loss due to an anomaly presumably
140 caused by material on the spacecraft outside the instrument that results in reduced coverage to
141 about half of its original swath as discussed in Section 2.4.](#)

142
143 The OMI NO₂ Standard Product (OMNO2) algorithm provides retrievals of NO₂ column (total,
144 tropospheric, and stratospheric) amounts by exploiting Level-1B calibrated radiance and irradiance
145 data from the Vis channel (350-500 nm with 0.63 nm spectral resolution). The algorithm employs
146 a multi-step procedure that consists of 1) a spectral fitting algorithm to calculate NO₂ slant column
147 densities (SCDs) as discussed in Section 2.1; 2) determination of air mass factors (AMFs) to
148 convert SCDs to vertical column densities (VCDs) as discussed in detail in Section 2.2; 3) a
149 scheme to remove cross-track dependent artifacts or stripes; and 4) a stratosphere-troposphere

150 separation scheme to derive tropospheric and stratospheric NO₂ VCDs. The AMF depends upon a
151 number of parameters including optical geometry (solar and viewing azimuth and zenith angles),
152 surface reflectivity, cloud pressure and fraction, and the shape of the NO₂ a priori vertical profile.

153 Since the first release of OMNO₂ in 2006 (Bucsela et al., 2006; Celarier et al., 2008), there have
154 been significant conceptual and technical improvements in the retrieval of NO₂ from space-based
155 measurements. Prior versions developed a new scheme for separating stratospheric and
156 tropospheric components in version 2.1 (V2.1) (Bucsela et al., 2013, Lamsal et al., 2014) and a
157 new algorithm for improved NO₂ SCD retrievals in V3.0 (Marchenko et al., 2015, Krotkov et al.,
158 2017), and included improved cloud products (Veefkind et al., 2016) in V3.1 (Choi et al., 2020).
159 The current version, V4.0, further improves on the retrievals in a number of significant ways for
160 NO₂ AMF and VCD calculations. Figure 1 shows a schematic diagram of the retrieval algorithm,
161 and Table 1 summarizes the differences and similarities between previous (V3.1) and current (V4)
162 versions. Some of the approaches in the V4 algorithm are similar to those used in V3.1, but there
163 are several important changes as discussed in detail in Sections 2.1 and 2.2.

164 **2.1 NO₂ and O₂-O₂ spectral fitting**

165 **2.1.1 NO₂ spectral fitting algorithm**

166 The spectral fitting algorithm for the operational standard OMI NO₂ product is described in detail
167 in Marchenko et al. (2015). Briefly, the algorithm retrieves NO₂ slant column densities (SCDs) by
168 using a Differential Optical Absorption Spectroscopy (DOAS) approach (e.g., Platt and Stutz,
169 2006). In the DOAS approach, laboratory-measured spectra of NO₂ (Vandaele et al., 1998) and
170 glyoxal (Volkamer et al., 2005), HITRAN08-based water vapor spectra (Rothman et al., 2009),
171 and rotational Raman (RR; Ring effect) filling-in are sequentially fitted to the OMI-measured
172 reflectance spectrum in the 402-465 nm wavelength range. The slant column represents the
173 integrated abundance of NO₂ along the average photon path from the Sun, through the atmosphere,
174 to the satellite. The Ring spectra are calculated as a linear combination of the atmospheric (Joiner
175 et al. 1995) and the liquid-water (Vasilkov et al., 2002) RR spectra, convolved with the wavelength
176 and cross-track dependent OMI transfer function (Dirksen et al., 2006). The algorithm employs a
177 multi-step, iterative retrieval procedure for removal of the Ring and spectral under-sampling
178 (Chance, et al., 2005) patterns as well as a low-order polynomial smoothing prior to estimation of
179 SCDs for all interfering species. This is in contrast with the conventional DOAS approach that

180 treats the Ring effect as a pseudo-absorber and fits all absorbers simultaneously with the
181 polynomial functions. For accurate wavelength shifts (radiances vs. irradiances), the standard
182 product algorithm splits the entire fitting window into seven carefully selected, partially
183 overlapping micro-windows, iteratively evaluates the RR spectrum amplitudes, performs
184 wavelength adjustments for each segment, and then iteratively retrieves the NO₂, H₂O, and glyoxal
185 in the windows best suited for a particular trace-gas species.

186 The OMI NO₂ SCDs from the standard product were compared with improved SCD retrievals
187 from the Quality Assurance for Essential Climate Variables (QA4ECV, <http://www.qa4ecv.eu/>),
188 BIRA-IASB's (Royal Belgian Institute for Space Aeronomy) QDOAS software ([http://uv-
189 vis.aeronomie.be/software/QDOAS/](http://uv-vis.aeronomie.be/software/QDOAS/)), and the latest KNMI retrievals (van Geffen et al., 2015) and
190 are shown to agree within 2% (Zara et al., 2018). The typical NO₂ SCD uncertainties amount to
191 $\sim 0.8 \times 10^{15}$ molec cm⁻², or 5-7% in high-SCD areas and 15-20% in low-SCD values (Marchenko et
192 al., 2015).

193 **2.1.2 O₂-O₂ spectral fitting algorithm**

194 The oxygen dimer (O₂-O₂) slant column fitting algorithm shares many features of the NO₂ fitting
195 algorithm and is described in detail in Vasilkov et al. (2018). It consists of a multi-step, iterative
196 retrieval approach with three carefully selected micro-windows sampling the flanks and the core
197 of the broad O₂-O₂ feature centered at 477 nm. The algorithm exploits OMI-measured reflectance
198 spectra in the 451-496 nm range to determine the wavelength shifts and RR amplitudes. The Ring
199 patterns are removed from the original OMI reflectances during the iterative adjustments for
200 differences in the wavelength registration of radiances and irradiances. The O₂-O₂ slant columns
201 are retrieved after removal of the NO₂ and H₂O absorptions estimated by the algorithm discussed
202 in the previous section, and of the ozone absorption using total ozone data from Veeffkind et al.
203 (2006). After removal of the interfering signals, the 477 nm O₂-O₂ absorption profile is carefully
204 normalized to the adjacent O₂-O₂ absorption-free reflectance levels accounting for very different
205 wavelength dependencies of surface reflectances over various geographical sites (e.g., the open-
206 ocean and desert area), as described in Vasilkov et al. (2018). The normalized O₂-O₂ absorption
207 profiles are then iteratively fitted with the temperature-dependent cross-sections from Thalman
208 and Volkamer (2013) over the 463-488 nm range to derive O₂-O₂ SCDs. These are used to estimate
209 the cloud properties as discussed below in Section 2.2.2.

210 **2.2 Improved air mass factor calculations**

211 The AMF, which is defined as the ratio of SCD to VCD, is needed to calculate the retrieved NO₂
212 VCD. Details of the AMF and its calculation are given in Palmer et al. (2001). The AMF for each
213 FOV is calculated by combining altitude (z)-dependent scattering weights (w) computed with a
214 radiative transfer model and a local a priori vertical NO₂ profile shape (S), taken from a chemistry-
215 transport model:

216
$$AMF = \int_{z_1}^{z_2} w(z)S(z)dz. \quad (1)$$

217 For the tropospheric AMF, the integral extends from the surface to the tropopause, whereas the
218 integral from the tropopause to the top of the atmosphere provides the stratospheric AMF. The
219 scattering weight at a given altitude describes the sensitivity of the backscattered radiation to the
220 abundance of the absorber at that altitude. For an optically thin absorber like NO₂, scattering
221 weights are a function of atmospheric scattering and are considered to be independent of the
222 species' vertical distribution (Palmer et al., 2001). Factors affecting scattering weights include
223 wavelength, optical geometry (solar and viewing azimuth and zenith angles), surface reflectivity,
224 and cloud pressure and fraction. The wavelength dependence of scattering weights is accounted
225 for by creating an average of scattering weights derived from the values at multiple wavelengths
226 within the NO₂ spectral fitting window. To compensate for the effect of the assumed constant NO₂
227 temperature (220 K) in the NO₂ SCD retrievals, the scattering weights are corrected for the
228 atmospheric temperature effect using local climatological monthly temperature profiles as
229 discussed in Bucseła et al. (2013). These profiles are based on the meteorological field from the
230 Modern-Era Retrospective Analysis for Research and Applications (MERRA-2) (Gelaro et al.,
231 2017).

232 The a priori NO₂ profile shapes are computed from a monthly mean climatology of vertical NO₂
233 profiles constructed from the Global Modeling Initiative (GMI) CTM simulation (Douglass et al.
234 2004, Strahan et al., 2007, Strode et al., 2015) driven by MERRA-2 meteorology. The spatial
235 resolution of the model is 1.25° in longitude and 1.0° in latitude, and the atmosphere is divided
236 into 72 pressure levels extending from the surface to 0.01 hPa. The model output is sampled
237 between 13:00 - 14:00, local time, consistent with the OMI overpass time. The use of monthly
238 NO₂ profiles helps capture the seasonal variation in the NO₂ vertical distribution (Lamsal et al.,
239 2010). The simulation is based on yearly varying NO_x emissions, as discussed in Strode et al.,
240 (2015); this is necessary to account for the effect of rapidly changing NO_x emissions (e.g., Tong

241 et al., 2015; Duncan et al., 2016; Miyazaki et al., 2017) on local NO₂ profile shapes (Lamsal et al.,
242 2015; Krotkov et al., 2017).

243 For each FOV, AMFs are computed for clear (AMF_{clr}) and cloudy (AMF_{cld}) conditions. The AMF
244 of a partially cloudy scene is calculated by assuming the independent pixel approximation:

$$245 \quad AMF = (1 - f_r) \times AMF_{clr} + f_r \times AMF_{cld}, \quad (2)$$

246 where f_r is the cloud radiance fraction (CRF), defined as the fraction of the measured radiation
247 that comes from clouds and scattering aerosols, and is computed at 440 nm from the retrieved
248 effective cloud fraction (ECF), f_c using Equation 8 (see below). AMF_{clr} is calculated for the
249 ground reflectivity of R_s and at terrain pressure P_s , whereas AMF_{cld} is calculated assuming a
250 Lambertian surface of reflectivity 0.8 at the retrieved cloud pressure. Below we provide a detailed
251 discussion of each of these input parameters that are incorporated in the OMNO2 V4.0 algorithm.

252 2.2.1 New surface reflectivity product for NO₂ and cloud retrievals

253 Surface reflectivity is an important input parameter for UV/Vis satellite retrievals of trace gases
254 and cloud information. The surface reflectance over both ocean and land depend upon viewing and
255 illumination geometry and can be accurately described by the bidirectional reflectance distribution
256 function (BRDF). This effect is, however, neglected by most currently available trace gas and
257 cloud algorithms which use a climatological Lambert-equivalent reflectivity (LER) for the surface.
258 To account for surface BRDF effects in the NO₂ and cloud retrievals, here we use the geometry-
259 dependent surface LER (GLER) product derived using the Moderate Resolution Imaging
260 Spectroradiometer (MODIS) BRDF data and the Vector Linearized Discrete Ordinate Radiative
261 Transfer (VLIDORT) calculation (Vasilkov et al., 2017; Qin et al., 2019; Fasnacht et al., 2019).
262 The GLER allows for a computationally efficient approach that does not require major changes to
263 the existing trace gas and cloud algorithms.

264 We derive GLER by inverting the top-of-atmosphere (TOA) radiance (I) of a Rayleigh atmosphere
265 over a non-Lambertian surface for each specific FOV and Sun-satellite geometry within the
266 Lambertian framework, i.e.,

$$267 \quad I = I_0 + GLER \times T / (1 - GLER \times S_b), \quad (3)$$

268 where I_0 is the TOA radiance calculated for a black surface, T is the total (direct + diffuse) solar
269 irradiance reaching the surface converted to the ideal Lambertian-reflected radiance (by dividing
270 by π steradians) and then multiplied by the transmittance of the reflected radiation between the

271 surface and TOA in the direction of a satellite instrument, and S_b is the diffuse flux reflectivity of
 272 the atmosphere for the case of its isotropic illumination from below (Dave, 1978). The value of I_0 ,
 273 T , and S_b are pre-computed with VLIDORT and stored in a look-up table. The GLER values are
 274 calculated at wavelengths relevant for both NO₂ (440 nm) and cloud (466 nm) retrievals.

275 Over land, the BRDF is calculated using the Ross-Thick Li-Sparse kernel model (Lucht et al.,
 276 2000) in VLIDORT (Spurr, 2006):

$$277 \quad BRDF = a_{iso} + a_{vol}k_{vol} + a_{geo}k_{vol}, \quad (4)$$

278 where the coefficients, a_{iso} , a_{vol} , and a_{geo} come from the Moderate Resolution Imaging
 279 Spectroradiometer (MODIS) Collection 5 gap-filled, seasonal snow-free BRDF product
 280 MCD43GF (Schaaf et al., 2002, 2011) for band 3 (459-479 nm) available at 30 arc-second spatial
 281 resolution and 8-day temporal resolution. The term a_{iso} is the isotropic contribution describing the
 282 Lambertian part of light reflection from the surface, the volumetric kernel (k_{vol}) describes light
 283 reflection from a dense leaf canopy, and the geometric kernel (k_{geo}) describes light reflection from
 284 a sparse ensemble of surface objects casting shadows on the background assumed to be
 285 Lambertian. The kernels are the only angle-dependent functions, the expressions of which are
 286 given in Lucht et al. (2000). The band 3 BRDF coefficients spatially averaged over an actual
 287 satellite FOV are used to calculate TOA radiance and GLER at 466 nm. To calculate GLER at 440
 288 nm, we apply a scaling method using the ratio of OMI-derived lambert equivalent reflectivity
 289 (LER) data at 440 nm and 466 nm:

$$290 \quad GLER_{440} = GLER_{466} \times f_s. \quad (5)$$

291 The value of $f_s = \frac{LER_{440}}{LER_{466}}$ is taken from the gridded monthly LER ratio data at 1°×1° or coarser
 292 resolution. The LER is determined from OMI TOA radiance measurements as discussed in
 293 Vasilkov et al. (2017, 2018). We use clear-sky (effective cloud fraction <0.02) and aerosol free
 294 (OMI UV Aerosol Index (Torres et al., 2007) <0.5) OMI LER data to create the monthly gridded
 295 data. The cloud and aerosol screening is necessary because the spectral dependence of surface
 296 features differ from that of clouds and aerosols.

297 Over water, the surface reflectance is calculated at the two wavelengths, 440 nm and 466 nm, using
 298 VLIDORT. To calculate TOA radiance, we include light specularly reflected from a rough water
 299 surface as well as diffuse light backscattered by water bulk. We also account for contributions
 300 from oceanic foam that can be significant for high wind speeds. Reflection from the water surface

301 is described by the Cox–Munk slope distribution function, which depends on both the wind speed
302 and the wind direction (Cox and Munk, 1954). Polarization at the ocean surface is accounted for
303 by using a full Fresnel reflection matrix as suggested by Mishchenko and Travis (1997).

304 We use wind speed data from a pair of satellite microwave imagers that include the Advanced
305 Microwave Scanning Radiometer - Earth Observing System (AMSR-E) instrument onboard the
306 NASA Aqua satellite (Wentz and Meissner, 2004) for 2004-2011 and the Special Microwave
307 Imager/Sounder (SSMIS) onboard the Air Force Defense Meteorological Satellite Program
308 (DMSP) Satellite F16 (Wentz et al., 2012) afterwards. Wind direction data are taken from the
309 Global Modeling Assimilation Office (GMAO) Goddard Earth Observing System Model Forward
310 Processing for Instrument Teams (GEOS-5 FP-IT) near real time assimilation.

311 Diffuse light from the ocean is described by a Case 1 water model with a single input parameter
312 of chlorophyll concentration (Morel, 1988) taken from the monthly Aqua/MODIS data. The
313 common Case 1 water model developed for the Vis (Morel, 1988) was extended to the UV using
314 data from Vasilkov et al. (2002, 2005). To calculate water-leaving radiance, we require the
315 downwelling irradiance at the surface (i.e., atmospheric transmittance). Since the transmittance
316 and the water-leaving contribution are coupled, we develop a simple coupling scheme in
317 VLIDORT that ensures the value of water-leaving radiance used as an input at the ocean surface
318 will correspond to the correct value of the downwelling flux reaching the surface interface
319 (Fasnacht et al., 2019).

320 For OMI ground pixels covering land and water surfaces, the TOA radiance (I) is calculated as an
321 average of radiance for land (I_L) and water (I_w) weighted by the pixel land fraction (f):

$$322 \quad I = fI_L + (1 - f)I_w. \quad (6)$$

323 The value of f is determined by converting various surface categories in the MODIS data (note
324 that these are of much higher spatial resolution than the OMI data) into a binary land-water mask
325 (e.g., treating all shorelines and ephemeral water as the land category and classifying all other
326 water sub-categories simply as water). The areal fraction of land (or water) for each OMI pixel is
327 then computed as the statistics of the binary categories.

328 Figure 2 shows an example of changes in surface reflectivity used in the previous (V3.1) and the
329 current (V4.0) version of the OMI NO₂ algorithm. The GLER data computed for OMI observations
330 as discussed above for March 20, 2005 differ considerably from the OMI-derived climatological

331 monthly LER data (Kleipool et al., 2008) for March. As shown in Figures 2 and 3(a), the GLERs
332 are generally lower than climatological LERs data except at swath edges with large viewing angles
333 and over areas affected by sunglint that correspond to higher values of GLER. Changes over the
334 sunglint areas are rather large, reaching up to 0.3. The climatological LER data derived by
335 analyzing histograms of five years of OMI-based LER data likely overestimate the actual surface
336 reflectivity due to residual cloud and aerosol contamination and underestimate over sunglint areas
337 as the procedure ignores sun glint affected observations. In contrast, the GLER data over land are
338 based on atmospherically corrected radiances from high-resolution MODIS observations,
339 minimizing the impact of both cloud and aerosols.

340 **2.2.2 Improved cloud products retrieval**

341 We develop a new algorithm that provides cloud parameters, namely cloud radiance fraction
342 (CRF) and cloud optical centroid pressure (OCP), and use them in the OMNO2 algorithm. Similar
343 to the standard OMCLDO2 algorithm (Veefkind et al, 2016), our cloud algorithm exploits the O₂-
344 O₂ absorption to retrieve O₂-O₂ SCD as discussed in Section 2.1.2, but derives the two cloud
345 parameters using the GLER and other ancillary data that are used in the NO₂ algorithm,
346 maintaining inter-algorithm consistency. The OMCLDO2 algorithm retrieves these parameters
347 using the climatological LER data from Kleipool et al. (2008). In the following, our new cloud
348 product is referred to as OMCDO2N.

349 The derivation of CRF and OCP is based on a simple cloud model called the mixed Lambertian-
350 equivalent reflectivity (MLER) model (Joiner and Vasilkov, 2006; Veefkind et al., 2016). The
351 MLER model treats cloud and ground as horizontally homogeneous, opaque Lambertian surfaces
352 and mixes them using the independent pixel approximation (IPA). According to the IPA, the
353 measured TOA radiance, I_m , is a sum of the clear-sky (I_g) and overcast (I_c) subpixel TOA
354 radiances that are weighted with an effective cloud fraction (ECF), f_c (e.g., Stammes et al., 2008):

$$355 \quad I_m = I_g(1 - f_c) + I_c f_c. \quad (7)$$

356 We choose the wavelength of 466 nm that is not substantially affected by rotational Raman
357 scattering (RRS) or atmospheric absorption to derive f_c . The parameters I_g and I_c are a function
358 of the ground and cloud LERs, respectively, and are calculated using VLIDORT (Spurr, 2006) and
359 obtained with an interpolated look up table. We use GLER discussed above for ground reflectivity

360 and a uniform cloud reflectivity of 0.8 (Koelemeijer et al., 2001; Stammes et al., 2008). The value
 361 of f_c is calculated by inverting Equation (7). Note that aerosols are implicitly accounted for in the
 362 determination of f_c , as they are treated (like clouds) as particulate scatters. CRF (f_r) defines the
 363 fraction of TOA radiance reflected by cloud:

$$364 \quad f_r = f_c \times \frac{I_c}{I_m}. \quad (8)$$

365 We use pre-computed look-up tables of the TOA radiances generated using VLIDORT. Due to its
 366 wavelength dependence, we calculate CRF at 466 nm for OCP at 440 nm for NO₂ retrievals.

367 The MLER model compensates for photon transport within a cloud by placing the Lambertian
 368 surface somewhere in the middle of the cloud instead of at the top (Vasilkov et al., 2008). The
 369 pressure of this surface corresponds to OCP, which can be modeled as a reflectance-averaged
 370 pressure level reached by backscattered photons (Joiner et al., 2012). We retrieve cloud OCP from
 371 the O₂-O₂ SCD discussed above (Section 2.1.2). The cloud OCP, P_c , is estimated by inversion
 372 using the MLER method to compute the appropriate O₂-O₂ AMFs:

$$373 \quad SCD = AMF_g \times VCD_g \times (1 - f_r) + AMF_c \times VCD_c \times f_r, \quad (9)$$

374 where VCD ($= SCD/AMF$) is the vertical column density of O₂-O₂ over ground (VCD_g) and cloud
 375 (VCD_c). The clear-sky (AMF_g) and overcast or cloudy (AMF_c) subpixel AMFs are calculated at
 376 477 nm with ground (GLER) and cloud (0.8) reflectivity, respectively. Look-up tables for the
 377 AMFs were generated using VLIDORT. Temperature profiles needed for estimation of VCD and
 378 AMF are taken from the GEOS-5 global data assimilation system (Rienecker et al., 2011).

379 In addition to OCP, we retrieve the so-called scene pressure. The scene pressure is derived from
 380 Eq. (9) assuming that $f_r = 1$ and cloud reflectivity = scene LER. The scene LER is determined
 381 from the measured TOA radiance using the equation (Eq. 3) that defines TOA radiance in the
 382 Rayleigh atmosphere over a Lambertian surface. In the absence of clouds, aerosols, and any major
 383 gas absorptions, the scene pressure should be equal to the surface pressure. The scene pressure is
 384 therefore an important diagnostic tool for evaluation of the performance of cloud pressure
 385 algorithms.

386 Figure 4 shows an example of cloud products retrieved with our algorithm compared with those
387 retrieved from the standard OMCLDO2 algorithm (Veefkind et al., 2016). The retrieved OCP and
388 CRF from the two algorithms exhibit broadly consistent spatial patterns in both cloud altitude and
389 amount. The values of OCP generally range from 370 hPa to 1001 hPa in OMCD02N versus 150
390 hPa to 1011 hPa in OMCLDO2N. For both products, CRF varies from 0 for clear-sky to 1 for
391 overcast conditions. A systematic difference is evident with generally higher values in OMCD02N
392 for OCP by 147 hPa and CRF by 0.01 as compared to OMCLDO2. For OCP, there is a general
393 pattern in difference with OMCD02N OCP higher for low-altitude clouds (>700 hPa) and lower
394 values for high-altitude clouds (<300 hPa) (Figure 3(c)). The largest OCP differences occur for
395 cases where cloud pressures in OMCLDO2 are clipped to 150 hPa. For CRF, larger differences
396 occur for partially cloudy scenes with higher CRF values in OMCD02N by 0-0.1 for both land
397 and water surfaces (Figure 3(b)). Exceptions are over sun-glint areas, where CRF in OMCD02N
398 is lower by 0-0.3 with the mean difference of 0.13.

399 **2.2.3 Treatment over snow and ice surfaces**

400 Over ice and snow surfaces, identified by the Near-real-time Ice and Snow Extent (NISE) flags
401 (Nolin et al., 2005) in the OMI Level 1b data, the following treatments are made for surface
402 reflectivity. In case of permanent ice and snow surfaces, the MCD43GF product provides BRDF
403 parameters, allowing us to calculate GLER. Over seasonal snow area usually with data gaps in
404 MCD43GF, we calculate OMI-derived LER but capped by a constant snow albedo of 0.6 following
405 Boersma et al. (2011). In rare cases of pixels not flagged by NISE and gaps in MODIS data, we
406 use OMI LER climatology (Kleipool et al., 2008), regardless whether the surface is either snow/ice
407 covered but missed by NISE or snow/ice free.

408 The OMI-derived scene reflectivity and scene pressure are used for NO₂ and cloud retrievals over
409 seasonal snow covered areas. If the NISE flags are set as true, the following assumptions are made
410 in our CRF, OCP, and NO₂ retrievals. Over bright surfaces (scene reflectivity > 0.2), we consider
411 the scenes as snow or cloud covered and assign the scene pressure to OCP. In addition, if a
412 difference between the surface pressure and scene pressure is smaller than 100 hPa, the scene is
413 considered to be either cloud free or covered by optically thin clouds following the cloud over
414 snow classification by Vasilkov et al. (2010), and CRF for the pixel is set to zero. If the difference
415 between the surface pressure and scene pressure exceeds 100 hPa, the scene is considered to be
416 overcast by optically thick (shielding) clouds (Vasilkov et al., 2010), and CRF for the pixel is set

417 to one. To avoid a possible NISE misclassification (Cooper et al., 2018) for low-reflectivity scenes
418 (scene reflectivity < 0.2), we consider such scenes as being snow/ice-free and calculate CRF, OCP,
419 and NO₂ AMF using the standard procedure with GLER for those scenes.

420 **2.2.4 Improved terrain height/pressure calculation**

421 Terrain pressure is a critical parameter to the AMF in NO₂ and cloud algorithms as well as to the
422 total optical depth of the Rayleigh atmosphere in the GLER algorithm. Prior studies have shown
423 that errors in terrain pressure can introduce over 20% errors in retrieved NO₂ VCD, especially in
424 areas of complex terrain (Zhou et al, 2010; Russell et al., 2011).

425 Here, we use a 2-arc minute Global Relief Model of global land-water surface data (ETOPOv2,
426 National Geophysical Data Center, 2006) to derive terrain height for each individual OMI ground
427 pixel. We derive the pixel-average terrain height by collocating and averaging the high resolution
428 data as discussed in Qin et al. (2019). The corresponding terrain pressure for each OMI pixel (P_s)
429 is calculated from the terrain pressure-height relationship established based on MERRA-2 monthly
430 terrain pressure (P_{s_GMI}) at a spatial resolution of 1° latitude × 1.25° longitude used in the GMI
431 model discussed above:

$$432 \quad P_s = P_{s_GMI} e^{-\left(\frac{\Delta z}{H}\right)}, \quad (10)$$

433 where $\Delta z (= z - z_{GMI})$ represents the difference between the average terrain height for an OMI
434 pixel (z) and the terrain height at GMI resolution (z_{GMI}). The parameter, $H = \frac{kT}{Mg}$, represents the
435 scale height, where k is the Boltzmann constant, T is the temperature at the surface, M is the mean
436 molecular weight of air, and g is the acceleration due to gravity.

437 **2.3 Impact of the changes on AMF**

438 Figure 5 shows an example of how changes in each individual input parameter affect tropospheric
439 AMFs which, in turn, translate inversely to tropospheric NO₂ column retrievals. Replacing
440 climatological LER from OMLER with daily GLER data affects scattering weight profiles in the
441 lower troposphere, resulting in lower values of tropospheric AMF almost everywhere, except over
442 sun glint areas, where the use of GLER enhances scattering weights and tropospheric AMF (Figure
443 5(a)). The changes in tropospheric AMF with GLER usually range from -50% to 25%,
444 occasionally reaching up to -100%. The effect is small (-6% to 1%) for overcast scenes (CRF>0.9),

445 and increases (-28% to 17%) over clear and partially cloudy scenes (CRF<0.5), for unpolluted
446 regions, and surges (-62% to 3%) over polluted areas ($>5 \times 10^{15}$ molec. cm^{-2}). Figure 6(a) shows
447 GLER-driven changes in clear-sky (CRF<0.5) tropospheric AMF for different surface and scene
448 types, separated by tropospheric NO_2 column amounts. For 80% of cases over land, 97% over
449 water outside of sunglint areas, and 98% over sunglint areas, tropospheric NO_2 columns are <
450 1.5×10^{15} molec. cm^{-2} and the average GLER-driven differences are small at $-6.6 \pm 17.3\%$, -
451 $3.8 \pm 7.1\%$, and $4.0 \pm 12.9\%$, respectively. The differences increase gradually with column amount
452 over NO_x source regions (e.g., cities and [highly polluted](#) coastal areas) with binned (of size 1×10^{15}
453 molec. cm^{-2}) average differences ranging from $-10 \pm 20.1\%$ to $-30 \pm 19.7\%$. Over snow and ice
454 surfaces, changes are rather large, reaching up to a factor of two. The impact of change in the
455 surface reflection data on stratospheric AMFs is negligible (<2%).
456 Figures 5(b) and 6(b) show how changes in the cloud parameters (CRF and OCP) affect
457 tropospheric AMF. Replacing OMCLDO2-based cloud parameters with those from OMCDO2N
458 changes scattering weight profiles in a complicated way. Higher values of OCP in OMCDO2N
459 will include [additional portions](#) of scattering weights [between the OMCDO2N- and OMCLDO2-](#)
460 [based OCPs, especially](#) in the lower troposphere, thereby reducing the tropospheric AMF. On the
461 other hand, the higher CRF values lead to an increased contribution of the cloudy AMF in the
462 calculation of tropospheric AMF, [thereby increasing its value](#). Their combination causes a wide
463 range of scenarios as well as large variation in the AMF effect. Overall, the change in cloud
464 parameters causes enhancement of tropospheric AMFs for partially cloudy and overcast scenes
465 and reduction for clear-sky scenes, especially over polluted areas. The AMF differences are
466 generally large for low AMF values that are driven by enhanced differences in either OCP, CRF,
467 or both as discussed in Vasilkov et al (2017). The changes in tropospheric AMF with the
468 OMCDO2N-based cloud parameters usually range from -17% to 28% with a larger variation over
469 land (-34% to 40%) as compared to water (-12% to 25%), and for low (<1) AMF (-47% to 41%)
470 as compared to high (>3) AMF (-4% to 18%). The largest changes in AMF (-96% to 62%) occur
471 over snow and ice surfaces that result from the difference in the treatment of snow and ice for
472 cloud and NO_2 retrievals as discussed in Section 2.2.3. For clear-sky and partially cloudy scenes
473 with CRF < 0.5, the effect of the changes in cloud parameters differs between land and water
474 surfaces as well as sunglint and non-sunglint geometries and becomes more pronounced over

Deleted: a larger portion

476 polluted land and coastal areas (Figure 6b). As in the case of surface reflectivity, the impact of the
477 change in cloud parameters on stratospheric AMF is <1%.

478 Figure 5c presents an example of changes in tropospheric AMF differences between the previous
479 approach of using terrain pressure at OMI pixel centers and the pixel average terrain pressure
480 implemented in the current version (V4.0). In general, the AMF changes driven by the changes in
481 terrain pressure are within $\pm 1\%$ over ocean and $\pm 3\%$ over land, although at times they can reach
482 up to 30%, especially for observations over complex terrain such as mountainous regions (Figure
483 5c inset).

484 Figures 5d and 6c show the AMF differences arising from the combined effect of changes in all
485 parameters discussed above. The effect arising from the replacement of the climatological OMLER
486 with GLER is partially compensated by the effect arising from the change in cloud parameters in
487 places where the two parameters exhibit opposite trend. Exceptions are over polluted land and
488 coastal areas, the GLER effect on AMF is augmented by the cloud effect. The average AMF
489 changes arising from all parameters (2%) are lower than the changes arising from either GLER (-
490 2.3%) or cloud parameters (4.1%), although the combined effect leads to a wider range of variation
491 in AMF changes (-100% to 57%) as compared to the effect from individual parameters. The
492 changes arising from all parameters are somewhat smaller (-21% to 34%) for overcast scenes
493 (CRF>0.9) as compared to (-47% to 29%) over clear and partially cloudy scenes (CRF<0.5), and
494 are substantial (-137% to 30%) over highly polluted areas ($>5 \times 10^{15}$ molec. cm⁻²) and over snow/ice
495 surfaces (-126% to 99%). Differences in the AMF effect are evident among land, water, and
496 sunglint areas (Figure 6c). The impact of the changes is below 1% for the stratospheric AMF.

497 2.4 Row anomaly and removal of stripes

498 The retrieved NO₂ SCDs have persistent relative biases in the 60 cross-track FOVs and show a
499 pattern of stripes running along each orbital track. This instrumental artifact is corrected using the
500 “de-striping” procedure described in detail in Bucsele et al (2013). Briefly, the de-striping
501 algorithm estimates the mean cross-track biases using measurements obtained at latitudes between
502 30S and 5N and from orbits within 2 orbits of target orbit. These correction values, one for each
503 cross-track position, are then subtracted from the retrieved SCDs to derive the de-striped SCD
504 field.

Deleted: is

Deleted: is

Deleted:

508 Starting June 25, 2007 and presumably even earlier, OMI experienced a more severe form of
509 anomaly that affects the quality of radiance data in certain rows at all wavelengths (Dobber et al.,
510 2008; Schenkeveld et al., 2017). This effect, called the “row anomaly” (RA), has developed and
511 changed over time. Currently, the RA has affected approximately half of the OMI’s FOVs,
512 resulting in OMI’s global coverage now in two days instead of one before the onset of the RA.

513 The quality of radiance data for the RA-affected FOVs is sufficiently poor as to prevent reliable
514 NO₂ retrievals. Therefore, we abandon retrieval calculations for all measurements that are flagged
515 by the RA-detection algorithm used in the Level-1 processing. We found that this RA-detection
516 algorithm may not be sufficiently sensitive to the relatively small (but important for our purposes)
517 RA changes. Figure 7 shows an example of anomalous rows not flagged by the RA-detection
518 algorithm but observed in the NO₂ retrievals. Shown are time series of average NO₂ SCDs
519 normalized by geometric AMFs over the Pacific Ocean for the RA-unaffected row of 20 (0-based)
520 compared with three rows that show significant degradation in the quality of SCD retrievals. These
521 particular rows are in the immediate proximity to the main RA area, thus showing the gradual RA
522 evolution: at the present epoch the RA slowly shifts towards the high-numbered rows – note the
523 sequential timing of the big drops in the retrievals in the rows 44-46. While the data from the three
524 rows start deviating from row 20 beginning from summer 2016, the data quality degrades further
525 for rows 44, 45, and 46 from September of 2017, 2018, and 2019, respectively, to the extent that
526 they cannot be sufficiently corrected by the de-stripping algorithm. In such cases, we implement
527 additional RA-flagging for those rows that start showing anomalous behavior, and exclude those
528 data from Level-2 and higher level NO₂ products.

529 2.5 Calculation of stratospheric and tropospheric NO₂ columns

530 We use an observation-based stratosphere-troposphere separation scheme to estimate the
531 stratospheric NO₂ field as discussed in detail in Bucsele et al. (2013), and the algorithm remains
532 unchanged in the current version. Briefly, the stratospheric field for an orbit is computed by
533 creating a gridded global field of initial stratospheric NO₂ VCD estimates (V_{init}) with data
534 assembled from within ± 7 orbits of the target orbit:

$$535 \quad V_{init} = \frac{S_{strat}}{AMF_{strat}} = \frac{S - S_{trop_{ap}}}{AMF_{strat}}. \quad (11)$$

536 Here S_{strat} and AMF_{strat} represent stratospheric SCD and AMF, respectively. An a priori
537 estimates of the tropospheric contribution ($S_{trop_{ap}}$) are subtracted from the measured, de-stripped

538 SCDs (S), and grid cells where this contribution exceeds 0.3×10^{15} molecules cm^{-2} are masked.
539 This masking ensures that the model contribution to the retrieval is minimal, especially in the
540 polluted areas. The residual field of the initial stratospheric VCDs measured outside the masked
541 regions mainly over unpolluted or cloudy areas is smoothed by a boxcar average and a 2-
542 dimensional interpolation, yielding an estimate for stratospheric NO_2 VCD (V_{strat}) for an
543 individual ground pixel.

544 The estimation of the stratospheric NO_2 VCD allows for the computation of the tropospheric NO_2
545 VCD (V_{trop}) from the de-stripped NO_2 SCD (S) and the tropospheric AMF (AMF_{trop}):

$$546 \quad V_{trop} = \frac{S_{trop}}{AMF_{trop}} = \frac{S - S_{strat}}{AMF_{trop}}, \quad (12)$$

547 where stratospheric NO_2 SCD (S_{strat}) is calculated from stratospheric AMF (AMF_{strat}) and V_{strat}
548 computed in the previous step.

549 With the updates in surface and cloud treatments as discussed in Section 2.2, the current version
550 has made significant improvements particularly in tropospheric AMFs and consequently in VCD
551 estimates. Further improvement to the retrievals is possible by enhancing the quality of a priori
552 NO_2 profiles [through improvements in model resolution, emissions, and chemistry](#), which remain
553 unchanged in the current version. If improved a priori NO_2 profiles become available, one can first
554 use Eq. 1 to readily re-calculate AMF_{trop} by combining them with scattering weights ($w(z)$)
555 archived in the data files and then use Eq. 12 together with other supplied parameters to re-
556 calculate V_{trop} . The same approach can be applied to remove the effect of a priori profiles used in
557 retrievals altogether, while comparing NO_2 columns from a model simulation with retrievals
558 [\(Eskes and Boersma, 2003; Lamsal et al., 2014\)](#).

559 Figure 8 shows a comparison of tropospheric and stratospheric NO_2 columns retrieved from V3.1
560 and V4.0 algorithms for 20 March, 2005. As expected, the updates implemented in V4.0 yield
561 higher (~ 10 – 40%) tropospheric NO_2 columns in polluted areas, with less-pronounced ($\pm 10\%$)
562 differences in background and low-column areas. These results are consistent with the observed
563 differences in the tropospheric AMF as discussed above in Section 2.2.4 as well as with other
564 previous regional studies over land surfaces (Zhou et al, 2010; McLinden et al, 2014; Lin et al.,
565 2014, 2015; Laughner et al., 2019; Liu et al., 2019) that implemented one or more of the changes
566 applied in V4.0. In contrast to changes in tropospheric NO_2 retrievals, changes in stratospheric
567 NO_2 estimates range between -3.6×10^{14} molec. cm^{-2} and 3.2×10^{14} molec. cm^{-2} and are close to the

568 range of expected uncertainties of stratospheric NO₂ estimates (Bucsela et al., 2013). The relative
569 differences in stratospheric NO₂ column between the two versions is close to 0% on average,
570 usually range between -2.5% and 2.0%, and occasionally reach up to ±13%. This difference in
571 stratospheric NO₂ estimates is much larger than the difference in stratospheric AMFs and is caused
572 by differences in tropospheric AMFs that influence NO₂ observations over unpolluted and cloudy
573 areas used by the stratosphere-troposphere separation scheme.

574 Figure 9 shows the seasonally averaged tropospheric NO₂ columns over the selected domains of
575 North America, Europe, southern Africa, and Asia for the months of June, July, and August in
576 2005. These domains contain highly polluted areas with significant NO_x emissions where the
577 impact of changes in surface reflectivity and cloud parameters on tropospheric NO₂ retrievals
578 becomes increasingly important. The use of more accurate pixel-specific information for surface
579 and cloud parameters in V4.0 results in significantly enhanced tropospheric NO₂ column retrievals
580 almost everywhere. The effect, however, varies with the vertical distribution of NO₂, with the
581 largest effects in high-column areas. This spatially-varying effect arising from algorithm changes
582 could have significant implications for estimates of trends and emissions of NO_x from satellite
583 observations.

584 Figure 10 shows the seasonal average tropospheric NO₂ columns for December through February.
585 While seasonal differences in NO₂ columns are evident owing to changes in NO_x lifetime and
586 boundary layer depth, the impact of algorithm changes in V4.0 remains similar. There are two
587 notable exceptions specifically related to observations over snow and ice surfaces. First, there are
588 significant data gaps in V3.1 but nearly none in V4.0. In V3.1, retrievals over snow and ice areas
589 were considered to be highly uncertain and therefore discarded, following the recommendation of
590 Boersma et al. (2011). As discussed above in Section 2.2.3, V4.0 incorporates changes in surface
591 and cloud treatment in NO₂ algorithm that allows us to retain more observations that we determine
592 to be our acceptable level of cloudiness. Next, these algorithm changes led to profound changes in
593 the calculated tropospheric AMFs and resulting NO₂ column amounts. The reduction in
594 tropospheric NO₂ retrievals in V4.0 over snow and ice covered surfaces arises from a combined
595 effect of enhanced values of surface reflectivity, their impact on the CRF and OCP retrievals, and
596 an inconsistent number of samples used in the calculation of the seasonal average. Nevertheless,
597 due to [inferiority in the quality of BRDF data as well as](#) complexities in separating snow from
598 clouds, caution is needed when interpreting winter time data at high latitudes.

Deleted: retrieved

600 [Figure 11 shows some examples of how changes in the algorithm from V3.1 to V4.0 affect monthly](#)
601 [domain average tropospheric NO₂ columns over areas affected by various NO_x sources. In contrast](#)
602 [to minor changes over the pristine Pacific Ocean, month-to-month changes over source regions](#)
603 [vary considerably. The differences in tropospheric NO₂ columns between V4.0 and V3.1 range](#)
604 [from -11 to 15% over Beijing, China and from 0 to 29% over the Ruhr area in Germany, suggesting](#)
605 [variations in relative differences among cities and industrial areas. The changes over a major](#)
606 [biomass burning area of Democratic Republic of Congo, Angola, and Zambia range 13-56%](#)
607 [during the biomass burning season of May through August, but are <5% in other months.](#)
608 [Differences between the two versions are small over areas influenced by lightning NO_x emissions.](#)
609
610 [In Figure 12, we examine monthly variation of tropospheric NO₂ columns from the two versions](#)
611 [over five highly populated and polluted cities that vary in terrain types ranging from coastal \(e.g.,](#)
612 [Shanghai, Tokyo\) to mountainous \(e.g., Mexico City\). NO₂ columns in V4.0 are generally higher](#)
613 [than V3.1 by 0-30%, but the difference can occasionally reach up to 50% in some months. Changes](#)
614 [of that order of magnitude in highly polluted areas have implications for estimation of NO_x](#)
615 [emissions and trends using these data.](#)

Formatted: Subscript

Formatted: Subscript

Formatted: Subscript

Formatted: Subscript

Formatted: Subscript

Formatted: Subscript

Formatted: Subscript

616 **3 Assessment of OMI NO₂ product**

617 In this section, we compare OMI NO₂ columns with total column retrievals from ground-based
618 Pandora measurements and integrated tropospheric columns from aircraft spirals at several
619 locations of the DISCOVER-AQ (Deriving Information on Surface Conditions from Column
620 and VERTically Resolved Observations Relevant to Air Quality) field campaign held between
621 2011 and 2014.

622 **3.1 Comparison between OMI and Pandora total column NO₂**

623 Here, we compare the total column NO₂ retrievals from OMI and the ground-based Pandora
624 spectrometer. Pandora is a compact sun-viewing remote sensing instrument that provides estimates
625 of NO₂ column amounts from the surface to the top of the atmosphere (Herman et al., 2009, 2018).
626 The NO₂ retrieval approach for Pandora is similar to that of OMI and consists of the DOAS spectral
627 fitting procedure to derive NO₂ SCD and its conversion to VCD using AMFs. However, the details

628 differ due to the lack of top-of-atmosphere radiance measurements for the spectral fitting and
629 simplicity in the AMF calculation for Pandora due to its direct sun measurements.

630 To compare with the OMI observations, we use Pandora data for sites listed in the Pandonia Global
631 Network (<https://www.pandonia-global-network.org/>). Out of 22 sites, we select 18 sites that we
632 determined to be suitable for comparison. Data from some of the sites (e.g., Rome, Italy) are
633 consistently higher than OMI by over a factor of two, suggesting that the sites may be in close
634 proximity to local sources that cannot be resolved by OMI. Although, some of the selected sites
635 have sporadic and short-term measurements (e.g., Ulsan, S. Korea), we consider them for
636 improved sampling and coverage. The collocation criteria include spatial and temporal matching
637 between OMI and Pandora observations by selecting the OMI pixels that encompass the Pandora
638 site and using Pandora 80-sec total NO₂ column data averaged over ±10 minutes of OMI
639 observations. We use high quality data obtained under clear sky conditions with root-mean-square
640 of spectral fitting residuals < 0.05 and NO₂ retrieval uncertainty < 0.05 DU (~1.3×10¹⁵ molec. cm⁻²)
641 for Pandora and with CRF < 0.5 for OMI.

642 Figure 13 shows a comparison of OMI total NO₂ columns (sum of tropospheric and stratospheric
643 columns) with coincidentally sampled Pandora direct-sun NO₂ column retrievals at a clean site of
644 Izaña in Tenerife Island, Spain, and a more polluted site in Greenbelt (Maryland, USA). The Izaña
645 Atmospheric Observatory is located on the top of a mountain plateau, with an elevation of 2373
646 meters above sea level. Since the site is free of local anthropogenic influences, Pandora
647 observations likely provide stratospheric and free tropospheric NO₂ amounts. In contrast, the
648 Greenbelt site in a suburban Washington DC area has traffic and air quality typical of polluted US
649 cities. As shown in Figures 13(a) and 13(b), OMI NO₂ retrievals from the two versions are highly
650 consistent (r>0.92) with somewhat higher values in V4.0 as compared to V3.1, by on average 13%
651 in Greenbelt and just 1% in Izaña. The variations of OMI NO₂ from both versions are also broadly
652 consistent with the Pandora measurements. The OMI and Pandora NO₂ columns are fairly
653 correlated (r = 0.32, N = 232) at Izaña, and moderately correlated (r = 0.51, N = 123) at Greenbelt;
654 often times the differences between each individual OMI and Pandora observations are significant.
655 Overall, the total column NO₂ data from OMI is higher than Pandora, with the average difference
656 of <16%. Occasional large discrepancies between OMI and Pandora reflect a combination of

Deleted: 1

Deleted: 1

Deleted: 1

660 spatial heterogeneity, differences in spatial and temporal sampling, differences in vertical
661 sensitivity of satellite and ground-based observations, and errors in OMI and Pandora retrievals.

662 Figures 13(c) and 13(d) show the multi-year monthly mean variation of OMI and Pandora NO₂
663 columns. The seasonal variation in Pandora and OMI NO₂ columns is highly consistent and
664 exhibits a summer maximum and a fall minimum at Izaña, and a winter maximum and summer
665 minimum in Greenbelt. The seasonal variation in the total column reflects that of the stratosphere
666 for Izaña and of the troposphere in Greenbelt. For Izaña, the monthly mean differences between
667 OMI and Pandora range from 8.2% in June to 38% in October for V4.0 and from 7.0% in June to
668 37% in October for V3.1. This discrepancy is likely due to the large aerial coverage of OMI pixels
669 including nearby cities, unlike the point measurements made by Pandora at the mountain top. The
670 average tropospheric NO₂ column observed by OMI is 8.9×10^{14} molec cm⁻², suggesting significant
671 NO₂ amounts in the troposphere with 20-32% contributions to total column NO₂ on a monthly
672 scale. For Greenbelt, the monthly mean differences between OMI and Pandora are within $\pm 12\%$
673 for the majority of the cases for both versions, with V4.0 improving agreement for February, April,
674 May and December, and worsening somewhat in other months, especially in September and
675 November, when the two versions exhibit larger differences in tropospheric NO₂ retrievals.

676 Figure 14 shows average total NO₂ columns measured by Pandora and OMI at the 18 selected
677 sites. Although there is a wide range of differences between individual sites, Pandora and OMI
678 observations exhibit a good spatial correlation, with slightly improved correlation for V4.0
679 ($r=0.65$, $N=1082$) as compared to V3.1 ($r=0.62$). The site-specific average values generally agree
680 to $\pm 35\%$ for columns $< 10^{16}$ molec. cm⁻². For more polluted sites, OMI retrievals tend to be lower
681 than the Pandora data. Although the relationship between Pandora and OMI has not changed
682 appreciably with the updates made in the OMI V4.0 product, the corrections are in the right
683 direction for a majority of the sites. The observed differences should not be interpreted as biases
684 in retrievals but rather as the combined effect of differences in spatial coverage, heterogeneity in
685 the NO₂ field, preferential placement of Pandora instruments, and potentially, a lack of site-
686 specific profile shapes assumed in OMI retrievals.

687 3.2 Assessment using DISCOVER-AQ observations

688 We also use NO₂ observations from the DISCOVER-AQ field program to assess V4.0 OMI NO₂
689 retrievals. The DISCOVER-AQ campaign was composed of four field deployments: Baltimore-
690 Washington area in Maryland (MD) in July 2011; the San Joaquin Valley in California (CA) in

Deleted: 1

Deleted: 1

Deleted: 2

694 January-February 2013; Houston, Texas (TX) in September 2013; and Denver, Colorado (CO) in
695 July-August 2014. An observing strategy of the campaign was to carry out systematic and
696 concurrent in situ and remote sensing observations from a network of ground sites and research
697 aircraft that spiraled over each site 2-4 times a day. The payload of the P-3B research aircraft
698 included in situ measuring instruments to measure NO₂ profiles in the 0.3-5 km altitude range.
699 Each campaign hosted ground-based networks of surface monitors to provide in situ NO₂
700 observations as well as Pandora spectrometers to measure NO₂ column amounts.

701 We use Pandora NO₂ column observations and in situ NO₂ spiral data spatially and temporally
702 matched to OMI on clear and partially cloudy (cloud radiance fraction < 0.5) days. Airborne
703 measurements were carried out using the 4-channel chemiluminescence instrument from the
704 National Center for Atmospheric Research (Ridley and Grahek, 1990) and the Thermal
705 Dissociation Laser-Induced Florescence from the University of Berkeley (Thornton et al., 2000).
706 Despite differences in the measurement technique and sampling strategy, NO₂ measurements from
707 the two instruments are highly consistent and generally agree within 10%, with the exception of
708 ~32% difference for Houston (Choi et al., 2020). Here, we use the 1-second merged data from the
709 chemiluminescence instrument only, taking advantage of its high frequency measurements. The
710 spiral data are extended to the ground by using coincident in situ surface NO₂ measurements
711 sampled over the duration of spiral (~20 minutes). To account for NO₂ amounts in the missing
712 portion from the highest aircraft altitude to the tropopause, we use NO₂ from the GMI simulation.
713 Like the surface data, the Pandora total column NO₂ data are averaged over the duration of each
714 aircraft spiral. For OMI, we include data from all cross-track positions that are not subject to the
715 row anomaly.

716 Figure 15 and Table 2 show a summary of the comparison of OMI V4.0 NO₂ columns with
717 vertically integrated tropospheric columns from the P-3B aircraft at 20 spiral locations. Overall,
718 tropospheric NO₂ columns from OMI and aircraft spirals suggest a poor agreement but a good
719 correlation ($r=0.74$, $N=100$), although the agreement and correlations vary by campaign locations
720 ($r=0.4$ for MD to $r=0.81$ for CA). OMI retrievals are usually lower than the aircraft data, with
721 larger differences for sites with larger NO₂ gradients and columns (e.g., Denver La Casa, CO;
722 Fresno, CA). OMI is rarely higher than the aircraft data as this usually happens over relatively
723 cleaner sites (e.g., Fairhill, MD). This alternating nature of the variation [in results in polluted](#)
724 [versus clean areas](#) suggests that OMI's large footprint size and narrow spiral radius (~4 km) of the

Deleted: 3

Deleted: s

727 aircraft are likely the primary cause for the observed differences. [This was](#) demonstrated in Choi
728 et al. (2020) by using high-resolution Community Multi-scale Air Quality Model (CMAQ)
729 simulations. Additional contributions to the observed differences could come from OMI retrieval
730 errors arising from the use of a coarse resolution GMI-based a priori NO₂ profile shapes in the
731 AMF calculation. Such profile-related retrieval errors can be partially accounted for by replacing
732 GMI profiles with the aircraft observed NO₂ profiles (OMI_{obs}). The use of observed profiles in the
733 OMI retrievals leads to a slight change in correlation, but [20-35% reduction in mean difference](#)
734 [between OMI and](#) aircraft observations, highlighting the role of a priori profiles in NO₂ retrievals
735 as suggested by previous studies (Russell et al., 2011; Lamsal et al., 2014; Goldberg et al., 2017;
736 Laughner et al., 2019; Choi et al., 2020). The campaign-average difference between OMI and
737 aircraft observations is -23.1%. We note here that the aircraft observed profiles can be very
738 different from the actual profiles over OMI's FOVs (pixels) due to a difference in the sampling
739 domains for the two measurements.

740 Figure 15, and Table 2 also show the comparison between the OMI and Pandora total column
741 retrievals at the 20 DISCOVER-AQ sites. The correlation between collocated OMI and Pandora
742 observations for individual campaign locations vary from fair ($r=0.13$ for MD) to good ($r=0.70$ for
743 CO), with a moderate correlation ($r=0.56$, $N=83$) for all observations from the four locations. As
744 compared to the aircraft observations, the OMI data generally show better agreement with the
745 Pandora retrievals, with the smallest difference in MD and the largest difference in CO. The use
746 of aircraft-observed NO₂ profiles in AMF calculations leads to higher OMI column retrievals than
747 those from Pandora for MD and TX, and lower columns than Pandora for CA and CO. Overall,
748 total column retrievals from OMI are 16.3% lower than Pandora. The observed discrepancy
749 between the OMI, aircraft spiral, and Pandora data points to general difficulties in comparing
750 observations of different spatial resolutions for a short-lived trace gas like NO₂ that has large
751 spatial gradients, especially in the boundary layer.

752 4 Conclusions

753 We have described a series of significant improvements made to the operational OMI NO₂
754 Standard Product (OMNO2) algorithm. The new version, version 4.0 (V4.0), of the OMNO2
755 product, released recently to the public at the NASA Goddard Earth Sciences Data and Information
756 Services Center (GES DISC), mainly relies on improved methods and high-resolution inputs for a
757 more accurate determination of air mass factors (AMFs). Major improvements include (1) a new

Deleted: significant (

Deleted:)

Deleted: improvements in agreement

Deleted: with

Deleted: 3

Deleted: s

764 O₂-O₂ cloud algorithm to estimate cloud radiance fraction (CRF) and cloud optical centroid
765 pressure (OCP), both required for the AMF calculation; 2) a new MODIS BRDF-derived
766 geometry-dependent surface Lambertian Equivalent Reflectivity (GLER) input data used in both
767 the NO₂ and cloud retrievals; (3) improved terrain pressure calculated for OMI's footprint; and (4)
768 improved surface and cloud treatments over snow and ice surfaces. Over open-water areas, inputs
769 to the GLER calculations include chlorophyll concentrations from MODIS, the wind speed data
770 from the Advanced Microwave Scanning Radiometer–Earth Observing System (AMSR-E) and
771 the Special Microwave Imager–Sounder (SSMIS) instruments, and the wind direction data from
772 the NASA GEOS-5 model. The following algorithmic steps remain unchanged: the scheme for
773 separating stratospheric and tropospheric components, first implemented in Version 2.1 (Bucsela
774 et al., 2013; Lamsal et al., 2014); an optimized spectral fitting algorithm used for NO₂ slant column
775 density retrievals (Marchenko et al., 2015); and the use of annually varying monthly mean Global
776 Modeling Initiative (GMI) derived inputs (e.g., NO₂ vertical profile shapes), as implemented in
777 Version 3.0 (Krotkov et al., 2017).

778 The changes in inputs result in substantial changes tropospheric AMFs (and thus VCDs) in V4.0
779 relative to the previous version (V3.1). The geometry-dependent GLER data computed for OMI
780 observations used in V4.0 differ considerably from the OMI-derived climatological LER data
781 (Kleipool et al., 2008) used in V3.1. The data from GLER (a unitless value with 0.0-1.0 range) are
782 generally lower, by <0.05, than the climatological LER data over land and ocean outside of
783 sunglint areas; ~~GLER is much higher over the sunglint areas that reaches more than 0.3 due to the~~
784 ~~geometry-dependent Fresnel reflection.~~ The cloud parameters (OCP and CRF) retrieved from by
785 new O₂-O₂ cloud algorithm described here and those from the operational cloud algorithm
786 (Veefkind et al., 2016) used in V3.1 exhibit significant differences with generally larger values for
787 both parameters in V4.0 as compared to V3.1, with noticeable exceptions over sunglint areas,
788 where CRFs in V4.0 are lower [than V3.1](#) by <0.3. Over snow and ice surfaces, identified by the
789 Near-real-time Ice and Snow Extent (NISE) flags in the OMI L1b data, various adjustments are
790 made in V4.0 for GLER, OCP, and CRF by using other diagnostic parameters (e.g., scene pressure)
791 retrieved by the new cloud algorithm. The scattering weights and tropospheric AMFs for NO₂
792 respond to the changes in these input parameters in a complicated way. Typically, tropospheric
793 AMFs decrease with the use of GLER and increase with the use of the new cloud parameters, with
794 exceptions over water surfaces affected by sunglint, where we observe the opposite effect. Over

- Deleted: , but
- Deleted: ,
- Deleted: ing
- Deleted: ,
- Deleted: proper modeling of

800 highly polluted areas, the effect from GLER is augmented by the effect from the new cloud
801 parameters, resulting in a considerable decrease in the tropospheric AMF. Changes in tropospheric
802 AMFs resulting from the updates in treatment of the snow and ice-covered areas are also
803 significant. Changes in the adopted terrain pressure (V4.0 vs V3.1) ~~can~~ also have a sizable effect
804 on tropospheric AMFs, particularly over areas with a complex terrain. In contrast, for stratospheric
805 AMFs the combined impact of all of these algorithmic updates is negligible.

Deleted: may

806 The changes in tropospheric AMFs translate directly into changes in tropospheric NO₂ retrievals
807 and indirectly into stratospheric NO₂ estimates. Over background and low column NO₂ areas,
808 tropospheric NO₂ column estimates have not changed appreciably from V3.1 to V4.0. Over more
809 polluted areas, the tropospheric NO₂ retrievals have typically increased by 10-40% from V3.1 to
810 V4.0, mostly in a direct proportion to the pollution level. Most of the increase in the highly polluted
811 areas is driven by the change in the surface reflectivity data used in the AMF calculation, with
812 additional increase due to changes in the cloud parameters. Changes in the stratospheric NO₂
813 estimates are usually within $\pm 2.5\%$, which is close to the range of estimated uncertainties of
814 stratospheric NO₂ estimates.

815 A global assessment of V4.0 tropospheric and stratospheric NO₂ products was performed by a
816 thorough evaluation of their consistency with the data from V3.1, which was carefully evaluated
817 in our previous works (e.g., Krotkov et al., 2017; Choi et al., 2020). In addition, we use
818 NO₂ measurements made by independent ground- and aircraft-based instruments to evaluate the
819 V4.0 product. The comparison of OMI total column NO₂ data with collocated Pandora
820 observations at its 18 global network and 20 DISCOVER-AQ locations suggests that OMI and
821 Pandora are generally highly consistent, exhibit similar seasonal variation, and agree within their
822 expected uncertainties of 2.7×10^{15} molec cm⁻² for Pandora (Herman et al., 2009) and $\sim 30\%$ for
823 OMI under clear-sky conditions (Boersma et al., 2011; Bucsela et al., 2013). Individual data points
824 differ considerably, and OMI tends to be lower than Pandora over highly polluted areas with
825 spatially inhomogeneous NO₂. The comparison of OMI tropospheric NO₂ column retrievals with
826 columns derived from the aircraft spirals and surface data during the DISCOVER-AQ campaign
827 also suggests general agreement in spatial variation, but OMI values are about a factor of two
828 lower in polluted environments. This difference is due partly to inaccurate a priori assumptions,
829 but primarily to OMI's ~~relatively~~ large pixels. The use of observed NO₂ profiles as a priori
830 information reduces the bias from $\sim 50\%$ to 23%, on average. The Multiple-Axis Differential

Deleted: relatively

833 Optical Absorption Spectrometer (MAX-DOAS) (e.g., Chan et al., 2019) or high spatial resolution
834 measurements from aircraft (e.g., Nowlan et al., 2016; Lamsal et al., 2017; Judd et al., 2019) would
835 provide a more comprehensive validation by mapping the NO₂ distributions over the complete
836 areas of aircraft spirals and the satellite FOVs.

837 In this study, we focused on improving the surface and cloud parameters in the NASA standard
838 NO₂ product retrievals. To further improve the retrieval accuracy, it is important to incorporate
839 improved retrieval methods and auxiliary information, such as high resolution a priori NO₂
840 profiles. For instance, current cloud algorithms based on the MLER model treat aerosols implicitly
841 by providing effective (cloud + aerosol) CRF and effective cloud OCP, both necessary inputs for
842 AMF calculations. Cloud effects on trace gas retrievals can be compromised by the unknown
843 aerosol effects, which lead to errors in AMF calculations. Therefore, the use of the GLER product
844 in the NO₂ algorithm will greatly benefit from an explicit accounting for aerosol effects,
845 particularly over polluted regions. We have recently developed an explicit and consistent aerosol
846 correction method which can be applied consistently in both the cloud and NO₂ retrievals
847 (Vasilkov et al. 2020); it uses a model of the aerosol optical properties from a global aerosol
848 assimilation system paired with radiative transfer calculations. This approach allows us to account
849 for aerosols within the OMI cloud and NO₂ algorithms with relatively small changes and will be
850 used in the next version of the NO₂ algorithm.

851

852 **Code/Data availability:** The Level-2 swath type column NO₂ products (OMNO2) is available
853 from the NASA Goddard Earth Sciences Data and Information Services Center (GES DISC)
854 website (https://disc.gsfc.nasa.gov/datasets/OMNO2G_003/summary). Other OMNO2-associated
855 NO₂ products such as the Level-2 gridded column product, OMNO2G, and the Level-3 gridded
856 column product, OMNO2d, both sampled at regular 0.25° latitude x 0.25° longitude wide grids are
857 distributed through the NASA GES-DISC
858 (https://disc.gsfc.nasa.gov/datasets/OMNO2d_003/summary) and GIOVANNI
859 (<https://giovanni.gsfc.nasa.gov/giovanni/>) websites. An additional high spatial resolution (0.1° x
860 0.1° latitude-longitude grid) OMNO2d product (OMNO2d_HR) is also made available through
861 the NASA AVDC website
862 (https://avdc.gsfc.nasa.gov/pub/data/satellite/Aura/OMI/V03/L3/OMNO2d_HR/). The AVDC

863 website also hosts overpass files for several hundred sites around the globe
864 (<https://avdc.gsfc.nasa.gov/pub/data/satellite/Aura/OMI/V03/L2OVP/OMNO2/>).

865

866 **Author contributions.** LNL, NAK, JJ, and AV designed the data analysis. WQ, ZF, NAK, DH,
867 and AV developed and evaluated the GLER product. EY, SM, AV, NAK, JJ, and BF developed
868 and evaluated the cloud product. LNL, NAK, SM, WHS, and EB have developed and evaluated
869 the NASA NO₂ Standard Product. LNL and SC conducted validation of the OMI NO₂ products
870 using Pandora and other independent observations. LNL, AV, SM, and ZF wrote the manuscript
871 with comments from all coauthors.

872

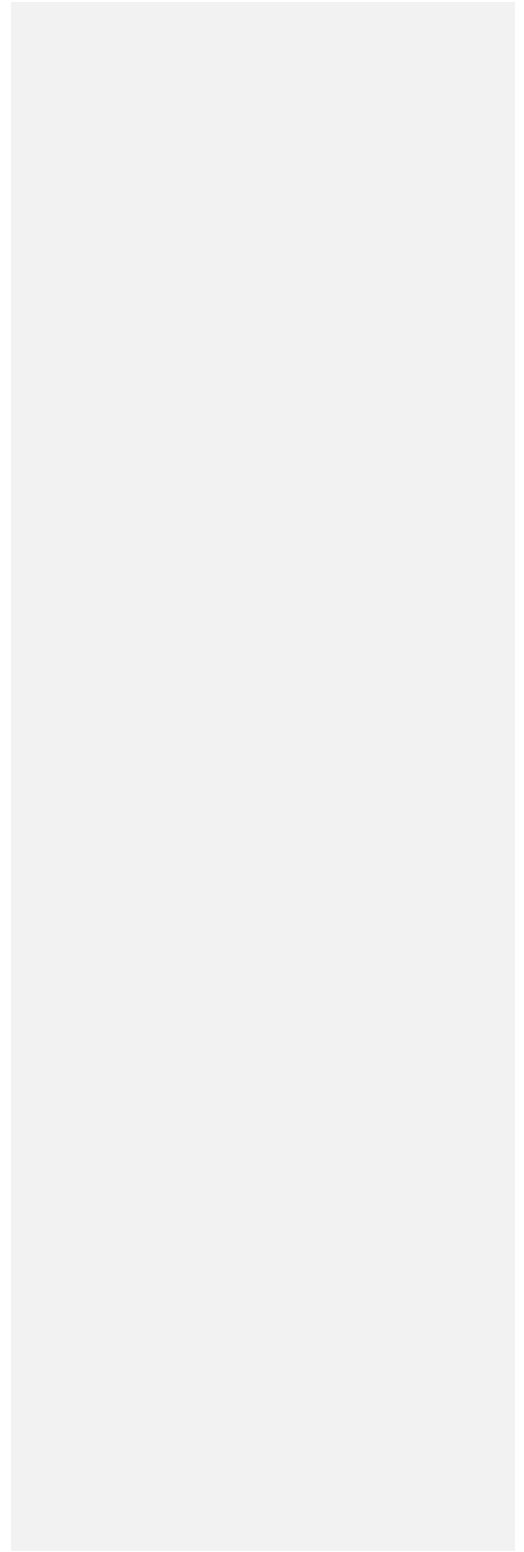
873 **Competing interests.** The authors declare no competing interests.

874

875 **Acknowledgements.** We acknowledge the NASA Earth Science Division for funding OMI NO₂
876 product development and analysis. The Dutch–Finnish-built OMI instrument is part of the NASA
877 EOS Aura satellite payload. KNMI and the Netherlands Space Agency (NSO) manage the OMI
878 project. We acknowledge the NASA Pandora, ESA-Pandonia, and NASA’s DISCOVER-AQ
879 projects for free access to the data. [We thank the two anonymous reviewers for their helpful](#)
880 [comments.](#)

881

30



882 **References**

- 883 Beirle, S., Boersma, K. F., Platt, U., Lawrence, M. G., and Wagner, T.: Megacity emissions and
884 lifetimes of nitrogen oxides probed from space, *Science*, 333, 1737–1739.
885 <https://doi.org/10.1126/science.1207824>, 2011.
- 886 Berezin, E. V., Kononov, I. B., Ciais, P., Richter, A., Tao, S., Janssens-Maenhout, G., et al.:
887 Multiannual changes of CO₂ emissions in China: indirect estimates derived from satellite
888 measurements of tropospheric NO₂ columns, *Atmos. Chem. Phys.*, 13, 9415–9438.
889 <https://doi.org/10.5194/acp-13-9415-2013>, 2013.
- 890 Boersma, K. F., Eskes, H. J., Dirksen, R. J., van der A, R. J., Veefkind, J. P., Stammes, P., Huijnen,
891 V., Kleipool, Q. L., Sneep, M., Claas, J., Leitão, J., Richter, A., Zhou, Y., and Brunner, D.:
892 An improved tropospheric NO₂ column retrieval algorithm for the Ozone Monitoring
893 Instrument, *Atmos. Meas. Tech.*, 4, 1905–1928, <https://doi.org/10.5194/amt-4-1905-2011>,
894 2011.
- 895 Boersma, K. F., Eskes, H. J., Richter, A., De Smedt, I., Lorente, A., Beirle, S., van Geffen, J. H.
896 G. M., Zara, M., Peters, E., Van Roozendaal, M., Wagner, T., Maasakkers, J. D., van der A,
897 R. J., Nightingale, J., De Rudder, A., Irie, H., Pinardi, G., Lambert, J.-C., and Compernelle,
898 S. C.: Improving algorithms and uncertainty estimates for satellite NO₂ retrievals: results
899 from the quality assurance for the essential climate variables (QA4ECV) project, *Atmos.*
900 *Meas. Tech.*, 11, 6651–6678, <https://doi.org/10.5194/amt-11-6651-2018>, 2018.
- 901 Bucsela, E.J., Celarier, E.A., Wenig, M.O., Gleason, J.F., Veefkind, J.P., Boersma, K.F., and
902 Brinkma, E.J.: Algorithm for NO₂ vertical column retrieval from the Ozone Monitoring
903 Instrument, *IEEE Trans. Geosci. Remote Sens.*, 44, 5, 2006.
- 904 Bucsela, E. J., Krotkov, N. A., Celarier, E. A., Lamsal, L. N., Swartz, W. H., Bhartia, P. K.,
905 Boersma, K. F., Veefkind, J. P., Gleason, J. F., and Pickering, K. E.: A new stratospheric and
906 tropospheric NO₂ retrieval algorithm for nadir-viewing satellite instruments: applications to
907 OMI, *Atmos. Meas. Tech.*, 6, 2607–2626, <https://doi.org/10.5194/amt-6-2607-2013>, 2013.
- 908 Cai, K., Li, S., Zheng, F., Yu, C., Zhang, X., Liu, Y., and Li, Y.: Spatio-temporal Variations in
909 NO₂ and PM_{2.5} over the Central Plains Economic Region of China during 2005-2015 Based
910 on Satellite Observations, *Aer. Air Qual. Res.*, 5, 1221–1235,
911 [10.4209/aaqr.2017.10.0394](https://doi.org/10.4209/aaqr.2017.10.0394), 2018.
- 912 Canty, T. P., Hembeck, L., Vinciguerra, T. P., Anderson, D. C., Goldberg, D. L., Carpenter, S.

913 F., Allen, D. J., Loughner, C. P., Salawitch, R. J., and Dickerson, R. R.: Ozone and NO_x
914 chemistry in the eastern US: evaluation of CMAQ/CB05 with satellite (OMI) data, *Atmos.*
915 *Chem. Phys.*, 19, 10965–10982, [10.5194/acp-15-10965-2015](https://doi.org/10.5194/acp-15-10965-2015), 2015.

916 Castellanos, P., and Boersma, K. F.: Reductions in nitrogen oxides over Europe driven by
917 environmental policy and economic recession, *Sci. Rep.*, 1, [10.1038/srep00265](https://doi.org/10.1038/srep00265), 2012.

918 Celarier, E. A., et al: Validation of Ozone Monitoring Instrument nitrogen dioxide columns, *J.*
919 *Geophys. Res.*, 113, D15S15, doi:[10.1029/2007JD008908](https://doi.org/10.1029/2007JD008908), 2008.

920 Chance, K., Kurosu, T.P., and Sioris, K.E.: Undersampling correction for array detector-based
921 satellite spectrometers, *Appl. Opt.*, 44, 1296–1304, 2005.

922 Chan, K. L., Wang, Z., Ding, A., Heue, K.-P., Shen, Y., Wang, J., Zhang, F., Shi, Y., Hao, N., and
923 Wenig, M.: MAX-DOAS measurements of tropospheric NO₂ and HCHO in Nanjing and a
924 comparison to ozone monitoring instrument observations, *Atmos. Chem. Phys.*, 19, 10051–
925 10071, <https://doi.org/10.5194/acp-19-10051-2019>, 2019.

926 Choi, S., Lamsal, L. N., Follette-Cook, M., Joiner, J., Krotkov, N. A., Swartz, W. H., Pickering,
927 K. E., Loughner, C. P., Appel, W., Pfister, G., Saide, P. E., Cohen, R. C., Weinheimer, A. J.,
928 and Herman, J. R.: Assessment of NO₂ observations during DISCOVER-AQ and KORUS-
929 AQ field campaigns, *Atmos. Meas. Tech.*, 13, 2523–2546, [https://doi.org/10.5194/amt-13-](https://doi.org/10.5194/amt-13-2523-2020)
930 [2523-2020](https://doi.org/10.5194/amt-13-2523-2020), 2020.

931 Cooper, M.J., Martin, R.V., Lyapustin, A.I., and McLinden, C.A.: Assessing snow extent data sets
932 over North America to inform and improve trace gas retrievals from solar backscatter, *Atmos.*
933 *Meas. Tech.*, 11, 2983-2994, <https://doi.org/10.5194/amt-11-2983-2018>, 2018.

934 Cox, C. and Munk, W.: Statistics of the sea surface derived from sun glitter, *J. Mar. Res.*, 13, 198–
935 227, 1954.

936 de Foy, B., Lu, Z., Streets, D. G., Lamsal, L. N., and Duncan, B. N.: Estimates of power plant NO_x
937 emissions and lifetimes from OMI NO₂ satellite retrievals. *Atmos. Environ.*, 116, 1–11,
938 <https://doi.org/10.1016/j.atmosenv.2015.05.056>, 2015.

939 Dirksen, R., Dobber, M., Voors, R., and Levelt, P.: Prelaunch characterization of the Ozone
940 Monitoring Instrument transfer function in the spectral domain, *Appl. Opt.*, 45, 3972–3981,
941 2006.

942 Dix, B., Bruin, J., Roosenbrand, E., Vlemmix, T., Francoeur, C., Gorchov-
943 Negron, A., McDonald, B., Zhizhin, M., Elvidge, C., Veeffkind, P., Levelt, P., and de Gouw,

944 J.: Nitrogen Oxide Emissions from U.S. Oil and Gas Production: Recent Trends and Source
945 Attribution, *Geophys. Res. Lett.*, 1, e2019GL085866, [10.1029/2019gl085866](https://doi.org/10.1029/2019gl085866), 2020.

946 Dobber, M., Kleipool, Q., Dirksen, R., Levelt, P. F., Jaross, G., Taylor, S., et al.: Validation of
947 Ozone Monitoring Instrument level 1b data products. *J. Geophys. Res.*,
948 <https://doi.org/10.1029/2007JD008665>, 2008.

949 Douglass, A. R., Stolarski, R.S., Strahan, S.E., and Connell, P.S.: Radicals and reservoirs in the
950 GMI chemistry and transport model: Comparison to measurements, *J. Geophys. Res.*, 109,
951 D16302, doi:[10.1029/2004JD004632](https://doi.org/10.1029/2004JD004632), 2004.

952 Duncan, B. N., Yoshida, Y., Foy, B., Lamsal, L. N., Streets, D. G., Lu, Z., Pickering, K. E., and
953 Krotkov, N. A.: The observed response of Ozone Monitoring Instrument (OMI) NO₂ columns
954 to NO_x emission controls on power plants in the United States: 2005–2011, *Atmos. Environ.*,
955 102–111, [10.1016/j.atmosenv.2013.08.068](https://doi.org/10.1016/j.atmosenv.2013.08.068), 2013.

956 Duncan, B.N., Lamsal, L.N., Thompson, A.M., Yoshida, Y., Lu, Z., Streets, D.G., Hurwitz, M.M.,
957 Pickering, K.E.: A space-based, high-resolution view of notable changes in urban NO_x
958 pollution around the world (2005–2014), *J. Geophys. Res.*, 121, 976–996,
959 doi:10.1002/2015JD024121, 2016.

960 [Eskes, H. J. and Boersma, K. F.: Averaging kernels for DOAS total-column satellite retrievals,](https://doi.org/10.5194/acp-3-1285-2003)
961 [Atmos. Chem. Phys.](https://doi.org/10.5194/acp-3-1285-2003), 3, 1285–1291, <https://doi.org/10.5194/acp-3-1285-2003>, 2003.

962 Fasnacht, Z., Vasilkov, A., Haffner, D., Qin, W., Joiner, J., Krotkov, N., Sayer, A. M., and Spurr,
963 R.: A geometry-dependent surface Lambertian-equivalent reflectivity product for UV–Vis
964 retrievals – Part 2: Evaluation over open ocean, *Atmos. Meas. Tech.*, 12, 6749–6769,
965 <https://doi.org/10.5194/amt-12-6749-2019>, 2019.

966 Geddes, J. A. and Martin, R. V.: Global deposition of total reactive nitrogen oxides from 1996 to
967 2014 constrained with satellite observations of NO₂ columns, *Atmos. Chem. Phys.*, 17,
968 10071–10091, <https://doi.org/10.5194/acp-17-10071-2017>, 2017.

969 Gelaro, R., McCarty, W., Suárez, M.J., Todling, R., Molod, A., Takacs, L., Randles, C.A.,
970 Darmenov, A., Bosilovich, M.G., Reichle, R., Wargan, K., Coy, L., Cullather, R., Draper, C.,
971 Akella, S., Buchard, V., Conaty, A., da Silva, A.M., Gu, W., Kim, G., Koster, R., Lucchesi,
972 R., Merkova, D., Nielsen, J.E., Partyka, G., Pawson, S., Putman, W., Rienecker, M., Schubert,
973 S.D., Sienkiewicz, M., and Zhao, B.: The Modern-Era Retrospective Analysis for Research
974 and Applications, Version 2 (MERRA-2). *J. Climate*, 30, 5419–

Formatted: Font: Italic

975 5454, <https://doi.org/10.1175/JCLI-D-16-0758.1>, 2017.

976 Ghude, S. D., Kulkarni, S. H., Jena, C., Pfister, G. G., Beig, G., Fadnavis, S., and A. R.
977 J.: Application of satellite observations for identifying regions of dominant sources of
978 nitrogen oxides over the Indian Subcontinent, *J. Geophys. Res.*, 2, 1075–
979 1089, [10.1029/2012jd017811](https://doi.org/10.1029/2012jd017811), 2013.

980 Goldberg, D. L., Lamsal, L. N., Loughner, C. P., Swartz, W. H., Lu, Z., and Streets, D. G.: A high-
981 resolution and observationally constrained OMI NO₂ satellite retrieval. *Atmos. Chem. Phys.*,
982 17, 11403–11421. <https://doi.org/10.5194/acp-17-11403-2017>, 2017.

983 Goldberg, D. L., Saide, P. E., Lamsal, L. N., de Foy, B., Lu, Z., Woo, J.-H., et al.: A top-down
984 assessment using OMI NO₂ suggests an underestimate in the NO_x emissions inventory in
985 Seoul, South Korea, during KORUS-AQ. *Atmos. Chem. Phys.*, 19, 1801–1818.
986 <https://doi.org/10.5194/acp-19-1801-2019>, 2019a.

987 Goldberg, D., Lu, Z., Oda, T., Lamsal, L.N, Liu, F., Griffin, D., McLinden, C., Krotkov, N.A.,
988 Duncan, B.N., Streets, D.: Exploiting OMI NO₂ satellite observations to infer fossil-fuel CO₂
989 emissions from U.S. megacities, *Sci. Tot. Environ.*, 695, 133805,
990 [10.1016/j.scitotenv.2019.133805](https://doi.org/10.1016/j.scitotenv.2019.133805), 2019b.

991 Gu, J., Chen, L., Yu, C., Li, S., Tao, J., Fan, M., Xiong, X., Wang, Z., Shang, H.,
992 and Su, L.: Ground-Level NO₂ Concentrations over China Inferred from the Satellite OMI
993 and CMAQ Model Simulations, *Rem. Sens.*, 6, 519, [10.3390/rs9060519](https://doi.org/10.3390/rs9060519), 2017.

994 Han, K., Lee, C., Lee, J., Kim, J., and Song, C.: A comparison study between model-predicted
995 and OMI-retrieved tropospheric NO₂ columns over the Korean peninsula, *Atmos.*
996 *Environ.*, 17, 2962–2971, [10.1016/j.atmosenv.2010.10.016](https://doi.org/10.1016/j.atmosenv.2010.10.016), 2011.

997 Herman, J., Cede, A., Spinei, E., Mount, G., Tzortziou, M., and Abuhassan, N.: NO₂ column
998 amounts from ground-based Pandora and MFDOAS spectrometers using the direct-sun
999 DOAS technique: Intercomparisons and application to OMI validation, *J. Geophys. Res.*
1000 *Atmos.*, 114, D13, <https://doi.org/10.1029/2009JD011848>,
1001 <https://agupubs.onlinelibrary.wiley.com/doi/abs/10.1029/2009JD011848>, 2009.

1002 Herman, J., Spinei, E., Fried, A., Kim, J., Kim, J., Kim, W., Cede, A., Abuhassan, N., and Segal-
1003 Rozenhaimer, M.: NO₂ and HCHO measurements in Korea from 2012 to 2016 from Pandora
1004 spectrometer instruments compared with OMI retrievals and with aircraft measurements
1005 during the KORUS-AQ campaign, *Atmos. Meas. Tech.*, 11, 4583–4603,

1006 <https://doi.org/10.5194/amt-11-4583-2018>, <https://www.atmos-meas->
1007 [tech.net/11/4583/2018/](https://www.atmos-meas-tech.net/11/4583/2018/), 2018.

1008 Herron-Thorpe, F. L., Lamb, B. K., Mount, G. H., and Vaughan, J. K.: Evaluation of a regional air
1009 quality forecast model for tropospheric NO₂ columns using the OMI/Aura satellite
1010 tropospheric NO₂ product, *Atmos. Chem. Phys.*, 18, 8839–8854, [10.5194/acp-10-8839-](https://doi.org/10.5194/acp-10-8839-2010)
1011 [2010](https://doi.org/10.5194/acp-10-8839-2010), 2010.

1012 Hudman, R. C., Moore, N. E., Mebust, A. K., Martin, R. V., Russell, A. R., Valin, L. C.,
1013 and Cohen, R. C.: Steps towards a mechanistic model of global soil nitric oxide emissions:
1014 implementation and space based-constraints, *Atmos. Chem. Phys.*, 16, 7779–
1015 7795, [10.5194/acp-12-7779-2012](https://doi.org/10.5194/acp-12-7779-2012), 2012.

1016 Ialongo, I., Herman, J., Krotkov, N., Lamsal, L., Boersma, K. F., Hovila, J., and Tamminen, J.:
1017 Comparison of OMI NO₂ observations and their seasonal and weekly cycles with ground-
1018 based measurements in Helsinki, *Atmos. Meas. Tech.*, 10, 5203–5212, [10.5194/amt-9-5203-](https://doi.org/10.5194/amt-9-5203-2016)
1019 [2016](https://doi.org/10.5194/amt-9-5203-2016), 2016.

1020 Joiner, J., Bhartia, P., Cebula, R., Hilsenrath, E., McPeters, R., and Park, H.: Rotational Raman
1021 scattering (Ring effect) in satellite backscatter ultraviolet measurements, *Appl. Opt.*, 34,
1022 4513–4525, 1995.

1023 Joiner J. and Vasilkov, A. P.: First Results from the OMI Rotational-Raman Scattering Cloud
1024 Pressure Algorithm, *IEEE Trans. Geophys. Remote Sens.*, 44, 1272–1282, 2006.

1025 Joiner, J., Vasilkov, A. P., Gupta, P., Bhartia, P. K., Veefkind, P., Sneep, M., de Haan, J., Polonsky,
1026 I., and Spurr, R.: Fast simulators for satellite cloud optical centroid pressure retrievals;
1027 evaluation of OMI cloud retrievals, *Atmos. Meas. Tech.*, 5, 529–545,
1028 <https://doi.org/10.5194/amt-5-529-2012>, 2012.

1029 Judd, L. M., Al-Saadi, J. A., Janz, S. J., Kowalewski, M. G., Pierce, R. B., Szykman, J. J., Valin,
1030 L. C., Swap, R., Cede, A., Mueller, M., Tiefengraber, M., Abuhassan, N., and Williams, D.:
1031 Evaluating the impact of spatial resolution on tropospheric NO₂ column comparisons within
1032 urban areas using high-resolution airborne data, *Atmos. Meas. Tech.*, 12, 6091–6111,
1033 <https://doi.org/10.5194/amt-12-6091-2019>, 2019.

1034 Kim, H. C., Lee, P., Judd, L., Pan, L., and Lefer, B.: OMI NO₂ column densities over North
1035 American urban cities: the effect of satellite footprint resolution, *Geos. Mod. Develop.*, 3,
1036 1111–1123, [10.5194/gmd-9-1111-2016](https://doi.org/10.5194/gmd-9-1111-2016), 2016.

1037 Kleipool, Q. L., Dobber, M. R., de Haan, J. F., and Levelt, P. F.: Earth surface reflectance
1038 climatology from 3 years of OMI data, *J. Geophys. Res.*, 113, D18308,
1039 doi:[10.1029/2008JD010290](https://doi.org/10.1029/2008JD010290), 2008.

1040 Koelemeijer, R. B. A., Stammes, P., Hovenier, J. W., and de Haan, J. F.: A fast method for
1041 retrieval of cloud parameters using oxygen A-band measurements from the Global Ozone
1042 Monitoring Experiment, *J. Geophys. Res.*, 106, 3475–3496, 2001.

1043 Konovalov, I. B., Berezin, E. V., Ciais, P., Broquet, G., Zhuravlev, R. V., and Janssens-Maenhout,
1044 G.: Estimation of fossil-fuel CO₂ emissions using satellite measurements of “proxy” species.
1045 *Atmos. Chem. Phys.*, 16(21), 13509–13540. <https://doi.org/10.5194/acp-16-13509-2016>,
1046 2016.

1047 Krotkov, N. A., McLinden, C. A., Li, C., Lamsal, L. N., Celarier, E. A., Marchenko, S.
1048 V., Swartz, W. H., Bucsela, E. J., Joiner, J., Duncan, B. N., Boersma, K.F., Pepijn, J.P.,
1049 Levelt, P.F., Fioletov, V.E., Dickerson, R. R., He, H., Lu, Z., and D. G. Streets, D.G.: Aura
1050 OMI observations of regional SO₂ and NO₂ pollution changes from 2005 to 2015, *Atmos.*
1051 *Chem. Phys.*, 7, 4605–4629, [10.5194/acp-16-4605-2016](https://doi.org/10.5194/acp-16-4605-2016), 2016.

1052 Krotkov, N. A., Lamsal, L. N., Celarier, E. A., Swartz, W. H., Marchenko, S. V., Bucsela, E. J., et
1053 al.: The version 3 OMI NO₂ standard product. *Atmos. Meas. Tech.*, 10, 3133–3149.
1054 <https://doi.org/10.5194/amt-10-3133-2017>, 2017.

1055 [Kuhlmann, G., Lam, Y. F., Cheung, H. M., Hartl, A., Fung, J. C. H., Chan, P. W., and Wenig, M.](#)
1056 [O.: Development of a custom OMI NO₂ data product for evaluating biases in a regional](#)
1057 [chemistry transport model. *Atmos. Chem. Phys.*, 15, 5627–5644, \[https://doi.org/10.5194/acp-\]\(https://doi.org/10.5194/acp-15-5627-2015\)](#)
1058 [15-5627-2015](#), 2015.

1059 Lamsal, L.N., Martin, R.V., van Donkelaar, A., Celarier, E.A., Bucsela, E.J., Boersma, K.F.,
1060 Dirksen, R., Luo, C., and Wang, Y.: Indirect validation of tropospheric nitrogen dioxide
1061 retrieved from the OMI satellite instrument: Insight into the seasonal variation of nitrogen
1062 oxides at northern midlatitude, *J. Geophys. Res.*, 115, doi:10.1029/2009JD013351, 2010.

1063 Lamsal, L.N., Martin, R.V., Parrish D.D., and Krotkov, N.A.: Scaling relationship for NO₂
1064 pollution and population size: A satellite perspective, *Environ. Sci. Technol.*, 47, 7855-7861,
1065 2013.

1066 Lamsal, L. N., Krotkov, N. A., Celarier, E. A., Swartz, W. H., Pickering, K. E., Bucsela, E. J.,
1067 Gleason, J. F., Martin, R. V., Philip, S., Irie, H., Cede, A., Herman, J., Weinheimer, A.,

Formatted: Font: Italic

1068 Szykman, J. J., and Knepp, T. N.: Evaluation of OMI operational standard NO₂ column
1069 retrievals using in situ and surface-based NO₂ observations, *Atmos. Chem. Phys.*, 14, 11587–
1070 11609, <https://doi.org/10.5194/acp-14-11587-2014>, 2014.

1071 Lamsal, L.N., Duncan, B.N., Yoshida, Y., Krotkov, N.A., Pickering, K.E., Streets, D.G., Lu, Z.:
1072 U.S. NO₂ trends (2005–2013): EPA Air Quality System (AQS) data versus improved
1073 observations from the Ozone Monitoring Instrument (OMI), *Atmos. Env.*, 110, pp:130-143,
1074 doi:10.1016/j.atmosenv.2015.03.055, 2015.

1075 Laughner, J. L., Zhu, Q., and Cohen, R. C.: Evaluation of version 3.0B of the BEHR OMI NO₂
1076 product. *Atmos. Meas. Tech.*, 12, 129–146. <https://doi.org/10.5194/amt-12-129-2019>, 2019.

1077 Laughner, J.J. and Cohen, R.C.: Direct observation of changing NO_x lifetime in North American
1078 cities, *Science*, 366, 6466, pp. 723-727, doi: 10.1126/science.aax6832, 2019.

1079 Levelt, P. F., van den Oord, G. H. J., Dobber, M. R., Dirksen, R. J., Malkki, A., Visser, H., de
1080 Vries, J., and Stammes, P.: The ozone monitoring instrument. *IEEE Trans. Geosci. Remote*
1081 *Sens.*, 44(5), 1093–1101. <https://doi.org/urn:nbn:nl:ui:25-648485>, 2006.

1082 Levelt, P. F., Joiner, J., Tamminen, J., Veeffkind, J. P., Bhartia, P. K., Stein Zweers, D. C., Duncan,
1083 B. N., Streets, D. G., Eskes, H., van der A, R., McLinden, C., Fioletov, V., Carn, S., de Laat,
1084 J., DeLand, M., Marchenko, S., McPeters, R., Ziemke, J., Fu, D., Liu, X., Pickering, K.,
1085 Apituley, A., González Abad, G., Arola, A., Boersma, F., Chan Miller, C., Chance, K., de
1086 Graaf, M., Hakkarainen, J., Hassinen, S., Ialongo, I., Kleipool, Q., Krotkov, N., Li, C.,
1087 Lamsal, L., Newman, P., Nowlan, C., Suleiman, R., Tilstra, L. G., Torres, O., Wang, H., and
1088 Wargan, K.: The Ozone Monitoring Instrument: overview of 14 years in space, *Atmos. Chem.*
1089 *Phys.*, 18, 5699–5745, <https://doi.org/10.5194/acp-18-5699-2018>, 2018.

1090 Lin, J.-T., Martin, R. V., Boersma, K. F., Sneep, M., Stammes, P., Spurr, R., Wang, P., Van
1091 Roozendaal, M., Clémer, K., and Irie, H.: Retrieving tropospheric nitrogen dioxide from the
1092 Ozone Monitoring Instrument: effects of aerosols, surface reflectance anisotropy, and vertical
1093 profile of nitrogen dioxide, *Atmos. Chem. Phys.*, 14, 1441–1461, [https://doi.org/10.5194/acp-](https://doi.org/10.5194/acp-14-1441-2014)
1094 [14-1441-2014](https://doi.org/10.5194/acp-14-1441-2014), 2014.

1095 Lin, J.-T., Liu, M.-Y., Xin, J.-Y., Boersma, K. F., Spurr, R., Martin, R., and Zhang, Q.: Influence
1096 of aerosols and surface reflectance on satellite NO₂ retrieval: seasonal and spatial
1097 characteristics and implications for NO_x emission constraints, *Atmos. Chem. Phys.*, 15,
1098 11217-11241, doi:10.5194/acp-15-11217-2015, 2015.

1099 Liu, F., Duncan, B. N., Krotkov, N. A., Lamsal, L. N., Beirle, S., Griffin, D., McLinden, C. A.,
1100 Goldberg, D. L., and Lu, Z.: A methodology to constrain carbon dioxide emissions from coal-
1101 fired power plants using satellite observations of co-emitted nitrogen dioxide, *Atmos. Chem.*
1102 *Phys.*, 20, 99–116, <https://doi.org/10.5194/acp-20-99-2020>, 2020.

1103 Liu, M.-Y., Lin, J.-T., Boersma, K. F., Pinardi, G., Wang, Y., Chimot, J., Wagner, T., Xie, P.,
1104 Eskes, H., Van Roozendaal, M., Hendrick, F., Wang, P., Wang, T., Yan, Y.-Y., Chen, L.-L.,
1105 and Ni, R.-J.: Improved aerosol correction for OMI tropospheric NO₂ retrieval over East Asia:
1106 constraint from CALIOP aerosol vertical profile, *Atmos. Meas. Tech.*, 12, 1-21,
1107 doi:10.5194/amt-12-1-2019, 2019.

1108 Lu, Z., Streets, D. G., de Foy, B., Lamsal, L. N., Duncan, B. N., and Xing, J.: Emissions of nitrogen
1109 oxides from US urban areas: Estimation from Ozone Monitoring Instrument retrievals for
1110 2005-2014, *Atmos. Chem. Phys.*, 15(18), 10367–10383. [https://doi.org/10.5194/acp-15-](https://doi.org/10.5194/acp-15-10367-2015)
1111 [10367-2015](https://doi.org/10.5194/acp-15-10367-2015), 2015.

1112 Lucht, W., Schaaf, C. B., and Strahler, A. H.: An algorithm for the retrieval of albedo from space
1113 using semiempirical BRDF models, *IEEE Trans. Geosci. Remote Sens.*, 38, 977–998, 2000.

1114 Marchenko, S., Krotkov, N. A., Lamsal, L. N., Celarier, E. A., Swartz, W. H., and Bucsela, E. J.:
1115 Revising the slant column density retrieval of nitrogen dioxide observed by the Ozone
1116 Monitoring Instrument, *J. Geophys. Res.*, 120, 5670–5692, 2015.

1117 Martin, R. V., Chance, K., Jacob, D.J., Kurosu, T.P., Spurr, R.J.D., Bucsela, E., Gleason, J.F.,
1118 Palmer, P.I., Bey, I., Fiore, A.M., Li, Q., Yantosca, R.M., Koelemeijer, R.B.A.: An improved
1119 retrieval of tropospheric nitrogen dioxide from GOME, *J. Geophys. Res.*, 107, 4437,
1120 doi:10.1029/2001JD001027, 2002.

1121 McLinden, C. A., Fioletov, V. E., Boersma, K. F., Kharol, S. K., Krotkov, N., Lamsal, L., et al.:
1122 Improved satellite retrievals of NO₂ and SO₂ over the Canadian oil sands and comparisons
1123 with surface measurements. *Atmos. Chem. Phys.*, 14, 3637–3656.
1124 <https://doi.org/10.5194/acp-14-3637-2014>, 2014.

1125 Mishchenko, M. I. and Travis, L. D.: Satellite retrieval of aerosol properties over the ocean using
1126 polarization as well as intensity of reflected sunlight, *J. Geophys. Res.*, 102, 16989–
1127 17013, <https://doi.org/10.1029/96JD02425>, 1997.

1128 Miyazaki, K., Eskes, H., Sudo, K., Boersma, K. F., Bowman, K., and Kanaya, Y.: Decadal
1129 changes in global surface NO_x emissions from multi-constituent satellite data

Formatted: Subscript

1130 assimilation, *Atmos. Chem. Phys.*, 2, 807–837, [10.5194/acp-17-807-2017](https://doi.org/10.5194/acp-17-807-2017), 2017.

1131 Montgomery, A., and Holloway, T.: Assessing the relationship between satellite-derived NO₂ and
1132 economic growth over the 100 most populous global cities, *J. Appl. Rem. Sens.*, 04, 1, [10.1117/1.jrs.12.042607](https://doi.org/10.1117/1.jrs.12.042607), 2018.

1133 Morel, A.: Optical modeling of the upper ocean in relation to its biogeochemical matter content (Case
1134 I waters), *J. Geophys. Res.*, 93, 10749–10768, <https://doi.org/10.1029/JC093iC09p10749>,
1135 1988.

1136 National Geophysical Data Center, 2006. 2-minute Gridded Global Relief Data (ETOPO2) v2.
1137 National Geophysical Data Center, NOAA. doi:10.7289/V5J1012Q [access
1138 date:2017/05/22].

1139 Nolin, A., Armstrong, R., and Maslanik, J.: Near real-time SSM/I EASE-grid daily global ice
1140 concentration and snow extent, Digit, Media, Natl. Snow Ice Data Center, Boulder, CO, USA,
1141 2005.

1142 Nowlan, C. R., Martin, R.V., Philip, S., Lamsal, L.N., Krotkov, N.A., Marais, E.A., Wang, S., and
1143 Zhang, Q.: Global dry deposition of nitrogen dioxide and sulfur dioxide inferred from space-
1144 based measurements, *Global Biogeochem. Cycles*, 28, 10, doi: 10.1002/2014GB004805,
1145 2014.

1146 Nowlan, C. R., Liu, X., Leitch, J. W., Chance, K., González Abad, G., Liu, C., Zoogman, P., Cole,
1147 J., Delker, T., Good, W., Murcray, F., Ruppert, L., Soo, D., Follette-Cook, M. B., Janz, S. J.,
1148 Kowalewski, M. G., Loughner, C. P., Pickering, K. E., Herman, J. R., Beaver, M. R., Long,
1149 R. W., Szykman, J. J., Judd, L. M., Kelley, P., Luke, W. T., Ren, X., and Al-Saadi, J. A.:
1150 Nitrogen dioxide observations from the Geostationary Trace gas and Aerosol Sensor
1151 Optimization (GeoTASO) airborne instrument: Retrieval algorithm and measurements during
1152 DISCOVER-AQ Texas 2013, *Atmos. Meas. Tech.*, 9, 2647–2668,
1153 <https://doi.org/10.5194/amt-9-2647-2016>, 2016.

1154 Palmer, P. I., Jacob, D. J., Fiore, A. M., and Martin, R. V., Air mass factor formulation for
1155 spectroscopic measurements from satellites: Application to formaldehyde retrievals from the
1156 Global Ozone Monitoring Experiment, *J. Geophys. Res.*, 106, 14539–
1157 514550, <https://doi.org/10.1029/2000JD900772>, 2001.

1158 Pickering, K.E., Bucseca, E., Allen, D., Ring, A., Holzworth, R., and Krotkov, N.A.: Estimates of
1159 lightning NO_x production based on OMI NO₂ observations over the Gulf of Mexico, *J.*
1160

1161 *Geophys. Res.*, 121, 14, pp 8668-8691, DOI: 10.1002/2015JD024179, 2016.

1162 Platt, U., and Stutz, J.: Differential optical absorption spectroscopy (DOAS), principle and
1163 applications, Springer Verlag, Heidelberg, 2006.

1164 Pope, R. J., Chipperfield, M. P., Savage, N. H., Ordóñez, C., Neal, L. S., Lee, L. A., Dhomse, S.
1165 S., Richards, N. A. D., and Keszlake, T. D.: Evaluation of a regional air quality model using
1166 satellite column NO₂: treatment of observation errors and model boundary conditions and
1167 emissions, *Atmos. Chem. Phys.*, 15, 5611–5626, <https://doi.org/10.5194/acp-15-5611-2015>,
1168 2015.

1169 Qin, W., Fasnacht, Z., Haffner, D., Vasilkov, A., Joiner, J., Krotkov, N., Fisher, B., and Spurr, R.:
1170 A geometry-dependent surface Lambertian-equivalent reflectivity product for UV–Vis
1171 retrievals – Part 1: Evaluation over land surfaces using measurements from OMI at 466 nm,
1172 *Atmos. Meas. Tech.*, 12, 3997–4017, <https://doi.org/10.5194/amt-12-3997-2019>, 2019.

1173 Rasool, Q. Z., Zhang, R., Lash, B., Cohan, D. S., Cooter, E. J., Bash, J. O., and Lamsal, L.
1174 N.: Enhanced representation of soil NO emissions in the Community Multiscale Air Quality
1175 (CMAQ) model version 5.0.2, *Geosci. Mod. Develop.*, 9, 3177–3197, [10.5194/gmd-9-3177-](https://doi.org/10.5194/gmd-9-3177-2016)
1176 [2016](https://doi.org/10.5194/gmd-9-3177-2016), 2016.

1177 Ridley, B. A. and Grahek, F. E.: A small, low flow, high sensitivity reaction vessel for NO
1178 chemiluminescence detectors, *J. Atmos. Oceanic Technol.*, 7, 307–311,
1179 [https://doi.org/10.1175/1520-0426\(1990\)0072.0.CO;2](https://doi.org/10.1175/1520-0426(1990)0072.0.CO;2), 1990.

1180 Rienecker, M. M., Suarez, M. J., Gelaro, R., Todling, R., Bacmeister, J., Liu, E., Bosilovich, M.
1181 G., Schubert, S. D., Takacs, L., Kim, G.-K., Bloom, S., Chen, J., Collins, D., Conaty, A., da
1182 Silva, A., Gu, W., Joiner, J., Koster, R. D., Lucchesi, R., Molod, A., Owens, T., Pawson, S.,
1183 Pegion, P., Redder, C. R., Reichle, R., Robertson, F. R., Ruddick, A. G., Sienkiewicz, M.,
1184 and Woollen, J.: MERRA: NASA's Modern-Era Retrospective Analysis for Research and
1185 Applications, *J. Clim.*, 24, 3624–3648, <https://doi.org/10.1175/JCLI-D-11-00015.1>, 2011.

1186 Rothman, L. S., Gordon, I.E., Barbe, A., Chris Benner, D., Bernath, P.F., Birk, M., Boudon, V.,
1187 Brown, L.R., Campargue, A., Champion, J.-P., Chance, K., Coudert, L.H., Dana, V., Devi,
1188 V.M., Fally, S., Flaud, J.-M., Gamache, R.R., Goldman, A., Jacquemart, D., Kleiner, I.,
1189 Lacome, N., Lafferty, W.J., Mandin, J.-Y., Massie, S.T., Mikhailenko, S.N., Miller, E.E.,
1190 Moazzen-Ahmad, N., Naumenko, O.V., Nikitin, A.V., Orphal, J., Perevalov, V.I., Perrin, A.,
1191 Predoi-Cross, A., Rinsland, C.P., Rotger, M., Šimečková, M., Smith, M.A.H., Sung, K.,

1192 Tashkun, S.A., Tennyson, J., Toth, R.A., Vandaele, A.C., Vander Auwera, J.: The HITRAN
1193 2008 molecular spectroscopic database, *J. Quant. Spectrosc. Radiat. Trans.*, 114, 533–572,
1194 2009.

1195 Russell, A. R., Perring, A. E., Valin, L. C., Bucsela, E. J., Browne, E. C., Wooldridge, P. J., and
1196 Cohen, R. C.: A high spatial resolution retrieval of NO₂ column densities from OMI: method
1197 and evaluation, *Atmos. Chem. Phys.*, 11, 8543–8554, [https://doi.org/10.5194/acp-11-8543-](https://doi.org/10.5194/acp-11-8543-2011)
1198 [2011](https://doi.org/10.5194/acp-11-8543-2011), 2011.

1199 Schaaf, C. B., Gao, F., Strahler, A. H., Lucht, W., Li, X., Tsang, T., Strugnell, N. C., Zhang, X.,
1200 Jin, Y., Muller, J.-P., Lewis, P., Barnsley, M., Hobson, P., Disney, M., Roberts, G.,
1201 Dunderdale, M., Doll, C., d’Entremont, R., Hu, B., Liang, S., and Privette, J. L.: First
1202 operational BRDF, albedo and nadir reflectance products from MODIS, *Rem. Sens. Environ.*,
1203 83, 135–148, 2002.

1204 Schaaf, C. L. B., Liu, J., Gao, F., and Strahler, A. H.: MODIS albedo and reflectance anisotropy
1205 products from Aqua and Terra, in: Land Remote Sensing and Global Environmental Change:
1206 NASA’s Earth Observing System and the Science of ASTER and MODIS, Remote Sensing
1207 and Digital Image Processing Series, edited by: Ramachandran, B., Justice, C., and Abrams,
1208 M., Vol. 11, Springer-Verlag, New York, 873 pp., 2011.

1209 Schenkeveld, V. M. E., Jaross, G., Marchenko, S., Haffner, D., Kleipool, Q. L., Rozemeijer, N.
1210 C., Veefkind, J. P., and Levelt, P. F.: In-flight performance of the Ozone Monitoring
1211 Instrument, *Atmos. Meas. Tech.*, 10, 1957–1986, <https://doi.org/10.5194/amt-10-1957-2017>,
1212 2017.

1213 Schreier, S. F., Richter, A., Kaiser, J. W., and Burrows, J. P.: The empirical relationship between
1214 satellite-derived tropospheric NO₂ and fire radiative power and possible implications for fire
1215 emission rates of NO_x, *Atmos. Chem. Phys.*, 5, 2447–2466, [10.5194/acp-14-2447-2014](https://doi.org/10.5194/acp-14-2447-2014), 2014.

1216 Shah, V., Jacob, D. J., Li, K., Silvern, R. F., Zhai, S., Liu, M., Lin, J., and Zhang, Q.: Effect of
1217 changing NO_x lifetime on the seasonality and long-term trends of satellite-observed
1218 tropospheric NO₂ columns over China, *Atmos. Chem. Phys. Disc.*, 1–23, [10.5194/acp-2019-](https://doi.org/10.5194/acp-2019-670)
1219 [670](https://doi.org/10.5194/acp-2019-670), 2019.

1220 Spurr, R. J. D.: VLIDORT: a linearized pseudo-spherical vector discrete ordinate radiative transfer
1221 code for forward model and retrieval studies in multilayer multiple scattering media, *J. Quant.*
1222 *Spectrosc. Rad. Trans.*, 102, 316–421, <https://doi.org/10.1016/j.jqsrt.2006.05.005>, 2006.

1223 Stammes, P., Sneep, M., de Haan, J. F., Veeffkind, J. P., Wang, P., and Levelt, P. F.: Effective
1224 cloud fractions from the Ozone Monitoring Instrument: Theoretical framework and
1225 validation, *J. Geophys. Res.*, 113, D16S38, <https://doi.org/10.1029/2007JD008820>, 2008.

1226 Strahan, S. E., Duncan, B.N., and Hoor, P.: Observationally derived transport diagnostics for the
1227 lowermost stratosphere and their application to the GMI chemistry and transport
1228 model, *Atmos. Chem. Phys.*, 7, 2435–2445, 2007.

1229 Strode, S.A., Rodriguez, J.M., Logan, J.A., Cooper, O.R., Witte, J.C., Lamsal, L.N., Damon, M.,
1230 Van Aartsen, B., Steenrod, S.D., and Strahan, S.E.: Trends and variability in surface ozone
1231 over the United States, *J. Geophys. Res.*, doi: 10.1002/2014JD022784, 2015.

1232 Tang, W., Cohan, D. S., Pour-Biazar, A., Lamsal, L. N., White, A.
1233 T., Xiao, X., Zhou, W., Henderson, B. H., and Lash, B. F.: Influence of satellite-derived
1234 photolysis rates and NO_x emissions on Texas ozone modeling, *Atmos. Chem. Phys.*, 4, 1601–
1235 1619, [10.5194/acp-15-1601-2015](https://doi.org/10.5194/acp-15-1601-2015), 2015.

1236 Thalman, R., and Volkamer, R.: Temperature dependent absorption cross-sections of O₂-O₂
1237 collision pairs between 340 and 630 nm and at atmospherically relevant pressure, *Phys.*
1238 *Chem. Chem. Phys.*, 15, 15371–15381, <https://doi.org/10.1039/C3CP50968K>, 2013.

1239 Thornton, J. A., Wooldridge, P. J., and Cohen, R. C.: Atmospheric NO₂: in situ laser-induced
1240 fluorescence detection at parts per trillion mixing ratios, *Anal. Chem.*, 72, 528–539,
1241 <https://doi.org/10.1021/ac9908905>, <https://doi.org/10.1021/ac9908905>, 2000.

1242 Tong, D., Lamsal, L.N., Pan, L., Kim, H., Lee, P., Chai, T., Pickering, K.E.: Long-term NO_x trends
1243 over large cities in the United States during the Great Recession: Intercomparison of satellite
1244 retrievals, ground observations, and emission inventories, *Atmos. Env.*, 109, doi:
1245 10.1016/j.atmosenv.2015.01.035, 2015.

1246 Torres, O., Tanskanen, A., Veihelman, B., Ahn, C., Braak, R., Bhartia, P. K., Veeffkind, V., and
1247 Levelt, P.: Aerosols and Surface UV Products from OMI Observations: An Overview, *J.*
1248 *Geophys. Res.*, 112, D24S47, <https://doi.org/10.1029/2007JD008809>, 2007.

1249 van der A, R. J., Eskes, H.J., Boersma, K.F., van Noije, T.P.C., Van Roozendaal, M., De Smedt, I.,
1250 Peters, D. H. M. U., and Meijer E.W.: Identification of NO₂ sources and their trends from
1251 space using seasonal variability analyses, *J. Geophys. Res.*, 113, D04302,
1252 doi:[10.1029/2007JD009021](https://doi.org/10.1029/2007JD009021), 2008.

1253 van Geffen, J. H. G. M., Boersma, K. F., Van Roozendaal, M., Hendrick, F., Mahieu, E., De Smedt,

1254 I., Sneep, M., and Veefkind, J. P.: Improved spectral fitting of nitrogen dioxide from OMI in
1255 the 405–465 nm window, *Atmos. Meas. Tech.*, 8, 1685–1699, [https://doi.org/10.5194/amt-8-](https://doi.org/10.5194/amt-8-1685-2015)
1256 1685-2015, 2015.

1257 Vandaele, A. C., Hermans, C., Simon, P.C., Carleer, M., Colin, R., Fally, S., Mérienne, M.F.,
1258 Jenouvrier, A., and Coquart, B.: Measurements of the NO₂ absorption cross-section from
1259 42,000 cm⁻¹ to 10,000 cm⁻¹ (238-1000 nm) at 220 K and 294 K, *J. Quant. Spectrosc. Radiat.*
1260 *Trans.*, 59, 171–184, 1998.

1261 Vasilkov, A., Joiner, J., Gleason, J., and Bhartia, P.K.: Ocean Raman scattering in satellite
1262 backscatter UV measurements, *Geophys. Res. Lett.*, 29, 1837, doi:[10.1029/2002GL014955](https://doi.org/10.1029/2002GL014955),
1263 2002.

1264 Vasilkov, A. P., Herman, J. R., Ahmad, Z., Karu, M., and Mitchell, B. G.: Assessment of the
1265 ultraviolet radiation field in ocean waters from space-based measurements and full radiative-
1266 transfer calculations, *Appl. Opt.*, 44, 2863–2869, <https://doi.org/10.1364/AO.44.002863>,
1267 2005.

1268 Vasilkov, A.P., Joiner, J., Spurr, R., Bhartia, P.K., Levelt, P., Stephens, G.: Evaluation of the OMI
1269 cloud pressures derived from rotational Raman scattering by comparisons with other satellite
1270 data and radiative transfer simulations, *J. Geophys. Res.*, 113, d15,
1271 <https://doi.org/10.1029/2007JD008689>, 2008.

1272 Vasilkov, A. P., Joiner, J., Haffner, D., Bhartia, P. K., and Spurr, R. J. D.: What do satellite
1273 backscatter ultraviolet and visible spectrometers see over snow and ice? A study of clouds
1274 and ozone using the A-train, *Atmos. Meas. Tech.*, 3, 619–629, [https://doi.org/10.5194/amt-3-](https://doi.org/10.5194/amt-3-619-2010)
1275 619-2010, 2010.

1276 Vasilkov, A., Qin, W., Krotkov, N., Lamsal, L., Spurr, R., Haffner, D., Joiner, J., Yang, E.-S., and
1277 Marchenko, S.: Accounting for the effects of surface BRDF on satellite cloud and trace-gas
1278 re-trievals: a new approach based on geometry-dependent Lambertian equivalent
1279 reflectivity applied to OMI algorithms, *Atmos. Meas. Tech.*, 10, 333–349,
1280 <https://doi.org/10.5194/amt-10-333-2017>, 2017.

1281 Vasilkov, A., Yang, E.-S., Marchenko, S., Qin, W., Lamsal, L., Joiner, J., Krotkov, N., Haffner,
1282 D., Bhartia, P.K., Spurr, R.: A cloud algorithm based on the O₂-O₂ 477 nm absorption band
1283 featuring an advanced spectral fitting method and the use of surface geometry-dependent
1284 Lambertian-equivalent reflectivity, *Atmos. Meas. Tech.*, 11, 4093-4107, doi: 10.5194/amt-11-

1285 4093-2018, 2018.

1286 Vasilkov, A., Krotkov, N., Yang, E.-S., Lamsal, L., Joiner, J., Castellanos, P., Fasnacht, Z., and
1287 Spurr, R.: Explicit and consistent aerosol correction for visible wavelength satellite cloud and
1288 nitrogen dioxide retrievals based on optical properties from a global aerosol analysis, *Atmos.*
1289 *Meas. Tech. Discuss.*, <https://doi.org/10.5194/amt-2019-458>, in review, 2020.

1290 Veefkind J. P., de Haan, J. F., Brinksma, E. J., Kroon, M., and Levelt, P. F.: Total ozone from the
1291 Ozone Monitoring Instrument (OMI) using the DOAS technique, *IEEE Trans. Geophys.*
1292 *Remote Sens.*, 44, 1239–1244, 2006.

1293 Veefkind, J. P., de Haan, J. F., Sneep, M., and Levelt, P. F.: Improvements to the OMI O₂–
1294 O₂ operational cloud algorithm and comparisons with ground-based radar–lidar observations,
1295 *Atmos. Meas. Tech.*, 9, 6035–6049, <https://doi.org/10.5194/amt-9-6035-2016>, 2016.

1296 Vinken, G. C. M., Boersma, K. F., Donkelaar, A., and Zhang, L., Constraints on ship NO_x
1297 emissions in Europe using GEOS-Chem and OMI satellite NO₂ observations, *Atmos. Chem.*
1298 *Phys.*, 3, 1353–1369, [10.5194/acp-14-1353-2014](https://doi.org/10.5194/acp-14-1353-2014), 2014a.

1299 Vinken, G. C. M., Boersma, K. F., Maasakkers, J. D., Adon, M., and Martin, R. V.: Worldwide
1300 biogenic soil NO_x emissions inferred from OMI NO₂ observations, *Atmos. Chem. Phys.*, 18,
1301 10363–10381, [10.5194/acp-14-10363-2014](https://doi.org/10.5194/acp-14-10363-2014), 2014b.

1302 Volkamer, R., Spietz, P., Burrows, J.P., and Platt, U., High-resolution absorption cross-section of
1303 Glyoxal in the UV/VIS and IR spectral ranges, *J. Photochem. Photobiol.*, 172, 35–46,
1304 doi:[10.1016/j.jphotochem.2004.11.011](https://doi.org/10.1016/j.jphotochem.2004.11.011), 2005.

1305 Meissner, T. and Wentz, F.J.: The Complex Dielectric Constant of Pure and Sea Water from
1306 Microwave Satellite Observations. *IEEE Trans. Geo. Rem. Sens.*, 42, 1836-1849.
1307 <http://dx.doi.org/10.1109/TGRS.2004.831888>, 2004.

1308 Wentz, F., Hilburn, K., and Smith, K.: RSS SSMIS ocean product grids daily from DMSP F16
1309 NETCDF. Dataset available online from the NASA Global Hydrology Resource Center
1310 DAAC, Huntsville, Alabama, USA, [https://doi.org/10.5067/MEASURES/DMSP-](https://doi.org/10.5067/MEASURES/DMSP-F16/SSMIS/DATA301)
1311 [F16/SSMIS/DATA301](https://doi.org/10.5067/MEASURES/DMSP-F16/SSMIS/DATA301), 2012.

1312 Zara, M., Boersma, K. F., De Smedt, I., Richter, A., Peters, E., van Geffen, J. H. G. M., Beirle, S.,
1313 Wagner, T., Van Roozendaal, M., Marchenko, S., Lamsal, L. N., and Eskes, H. J.: Improved
1314 slant column density retrieval of nitrogen dioxide and formaldehyde for OMI and GOME-2A
1315 from QA4ECV: intercomparison, uncertainty characterisation, and trends, *Atmos. Meas.*

1316 *Tech.*, 11, 4033–4058, <https://doi.org/10.5194/amt-11-4033-2018>, 2018.

1317 Zhou, Y., Brunner, D., Spurr, R. J. D., Boersma, K. F., Sneep, M., Popp, C., and Buchmann, B.:

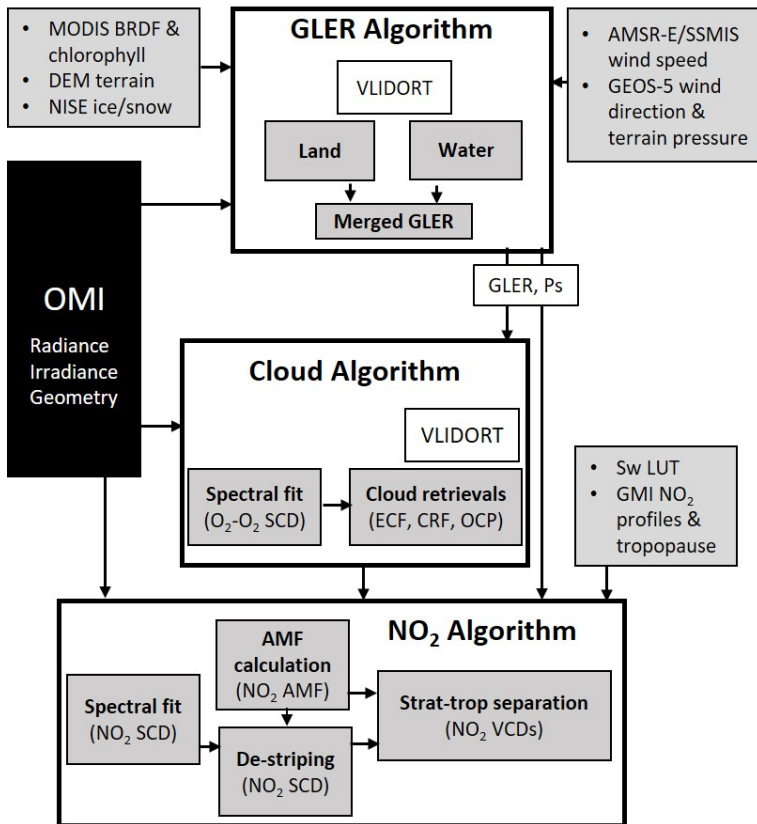
1318 Accounting for surface reflectance anisotropy in satellite retrievals of tropospheric NO₂,

1319 *Atmos. Meas. Tech.*, 3, 1185–1203, <https://doi.org/10.5194/amt-3-1185-2010>, 2010.

1320 Zhou, Y., Brunner, D., Hueglin, C., Henne, S., and Stachelin, J.: Changes in OMI tropospheric

1321 NO₂ columns over Europe from 2004 to 2009 and the influence of meteorological

1322 variability, *Atmos. Environ.*, 482–495, [10.1016/j.atmosenv.2011.09.024](https://doi.org/10.1016/j.atmosenv.2011.09.024), 2012.



1323

1324 **Figure 1:** Schematic diagram of the NASA OMI NO₂ algorithm, version 4.0, which is coupled

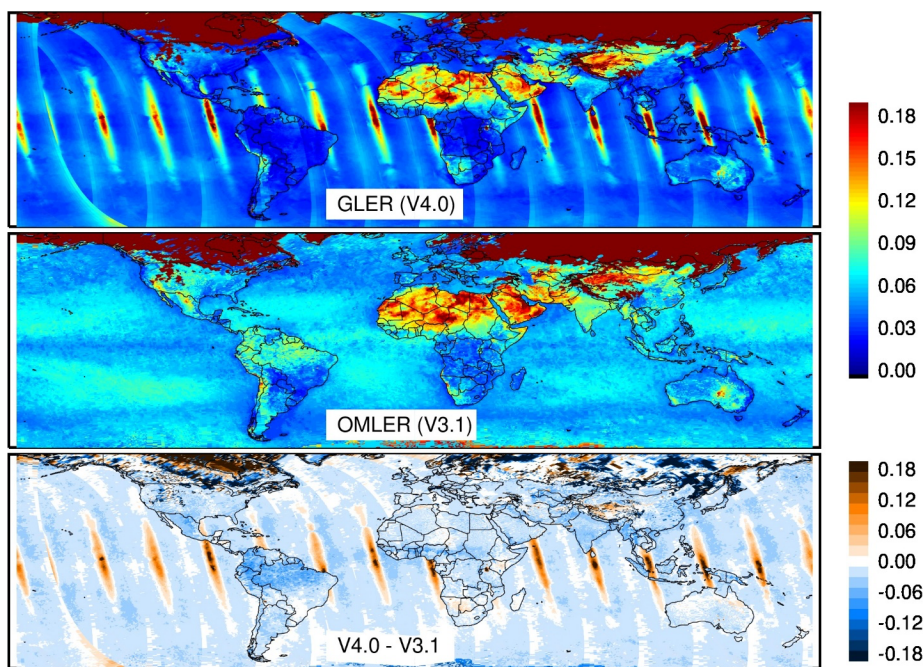
1325 with the cloud and geometry-dependent surface Lambertian Equivalent Reflectivity (GLER)

1326 algorithms that ultimately produces stratospheric (strat) and tropospheric (trop) NO₂ vertical

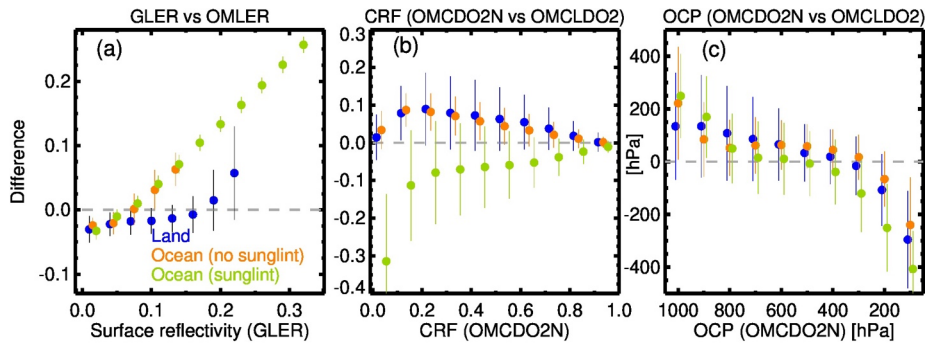
1327 column densities (VCDs). Acronyms used here are described in relevant sections below.

1328 VLIDORT: Vector Linearized Discrete Ordinate Radiative Transfer; MODIS: Moderate

1329 Resolution Imaging Spectro-radiometer; BRDF: bidirectional reflectance distribution function;
 1330 DEM: Digital Elevation Model; NISE: Near-real-time Ice and Snow Extent; AMSR-E: Advanced
 1331 Microwave Scanning Radiometer for Earth Observing System (EOS); SSMIS: Special Sensor
 1332 Microwave Imager / Sounder; GEOS-5: Goddard Earth Observing System, Version 5; [Ps: surface](#)
 1333 [\(terrain\) pressure over OMI pixel](#); ECF: Effective Cloud Fraction; CRF: Cloud Radiance Fraction;
 1334 OCP: Optical Centroid Pressure; Sw: Scattering weight; LUT: Look-up table GMI: Global
 1335 Modeling Initiative; AMF: Air Mass Factor; SCD: Slant Column Density.
 1336



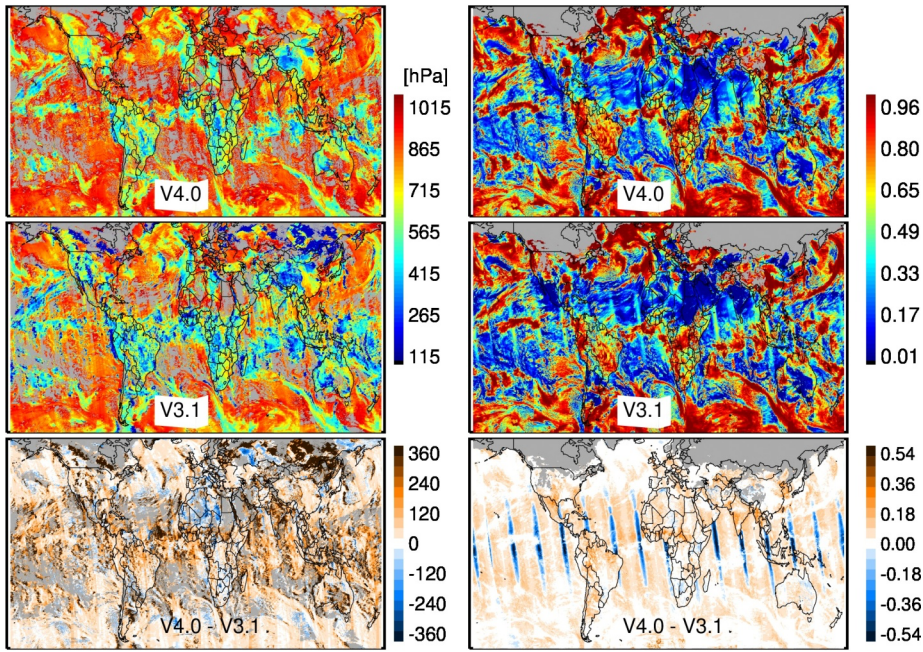
1337
 1338 **Figure 2:** Surface reflectivity at 440 nm (top) derived using MODIS BRDF data with OMI
 1339 geometry (GLER) on March 20, 2005 compared with (middle) OMI-based monthly LER
 1340 climatology (OMLER) for the month of March (Kleipool et al., 2008). The bottom panel shows
 1341 the difference between MODIS-based and climatological surface reflectivity data.



1342

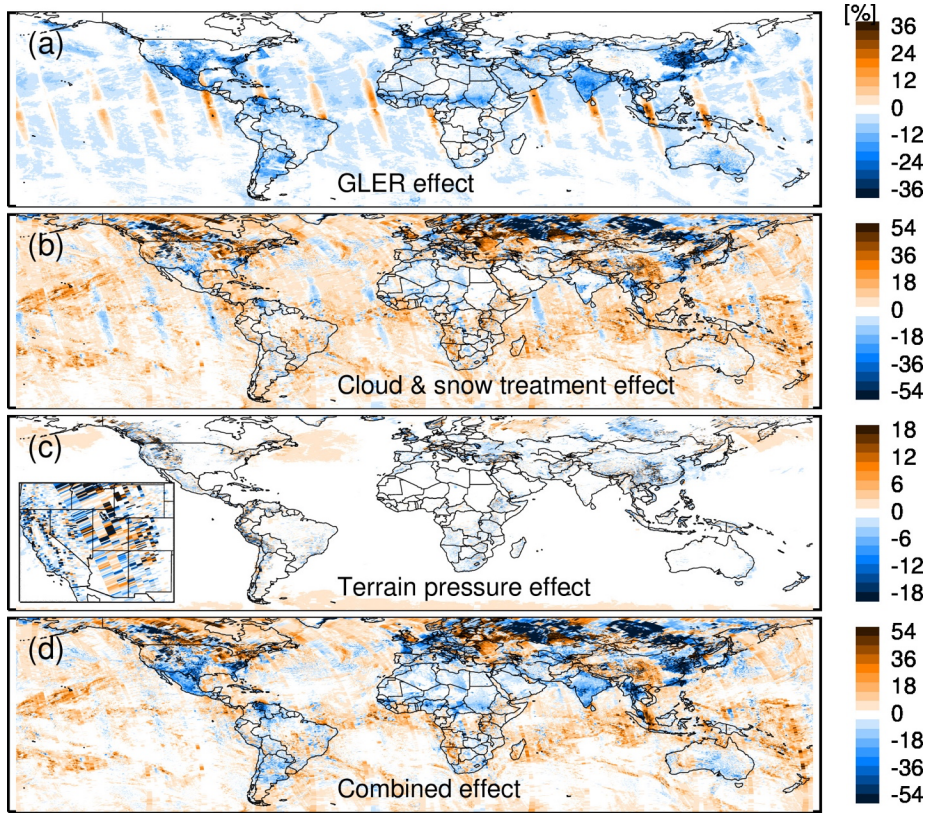
1343 **Figure 3:** Differences (V4.0 – V3.1) in (a) surface reflectivity, (b) cloud radiance fraction, and (c)
 1344 cloud optical centroid pressure for March 20, 2005, as used in V3.1 and V4.0 algorithms and
 1345 binned by the values of corresponding parameters from V4.0. Data are separated for land (blue)
 1346 and ocean surfaces, and by sunglint (green) and non-sunglint (orange) geometry over ocean. The
 1347 vertical bars represent the standard deviation for each bin of those parameters.

1348



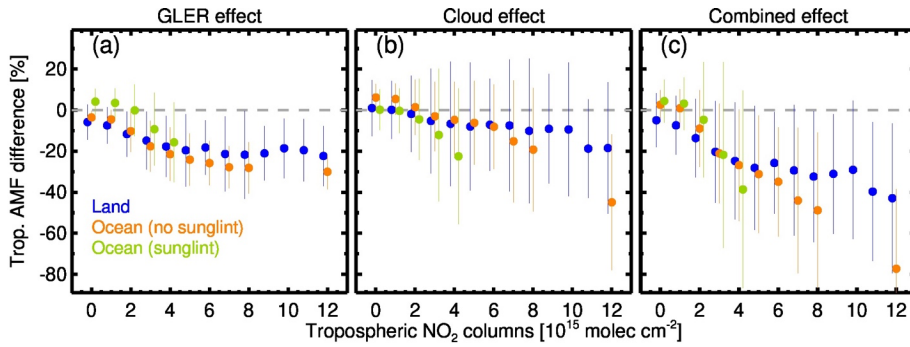
1349

1350 **Figure 4:** Cloud optical centroid pressure at 477 nm (left) and cloud radiance fraction at 440 nm
 1351 (right) retrieved for March 20, 2005 with OMNO2 V4.0 (top) and V3.1 (middle) algorithms,
 1352 respectively. The bottom rows show their differences. The gray color represents the OMI pixels
 1353 with retrieved cloud pressure equal to terrain pressure in V4.0 on the left and over snow/ice surface
 1354 identified by the NISE flag on the right.



1355

1356 **Figure 5:** Impact on tropospheric AMF (i.e., V4.0 – V3.1) from changes in (a) surface reflectivity,
 1357 (b) cloud and surface treatment, (c) terrain pressure, and (d) their combination on March 20, 2005.
 1358 The figure 5(c) inset shows zoomed view of impact over complex terrain in the western US.



1359

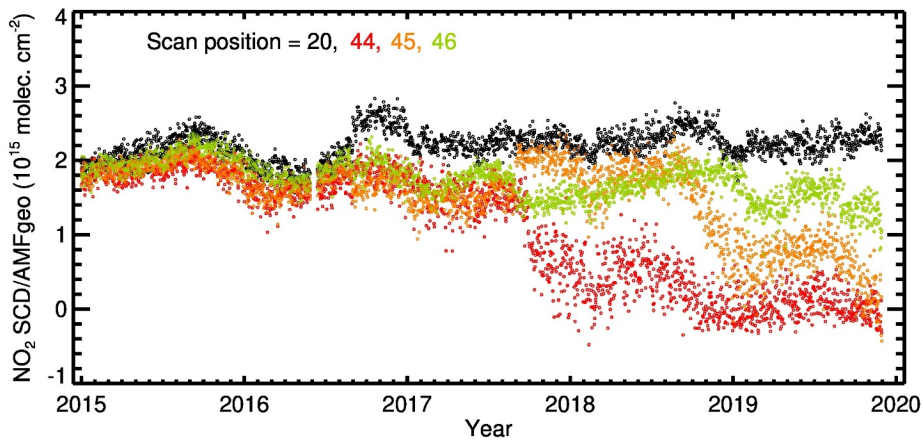
1360 **Figure 6:** The impact on tropospheric AMF (i.e., V4.0 – V3.1) from changes in (a) surface
 1361 reflectivity, (b) cloud, and (c) their combination for clear and partially cloudy scenes (CRF<0.5)
 1362 on March 20, 2005. Percent differences in tropospheric AMF are sorted by tropospheric NO₂
 1363 columns, separating them by land (blue) and ocean, and by sunglint (green) and non-sunglint
 1364 (orange) geometry over ocean. The vertical bars represent the standard deviations for the
 1365 tropospheric NO₂ column bins.

1366

1367

1368

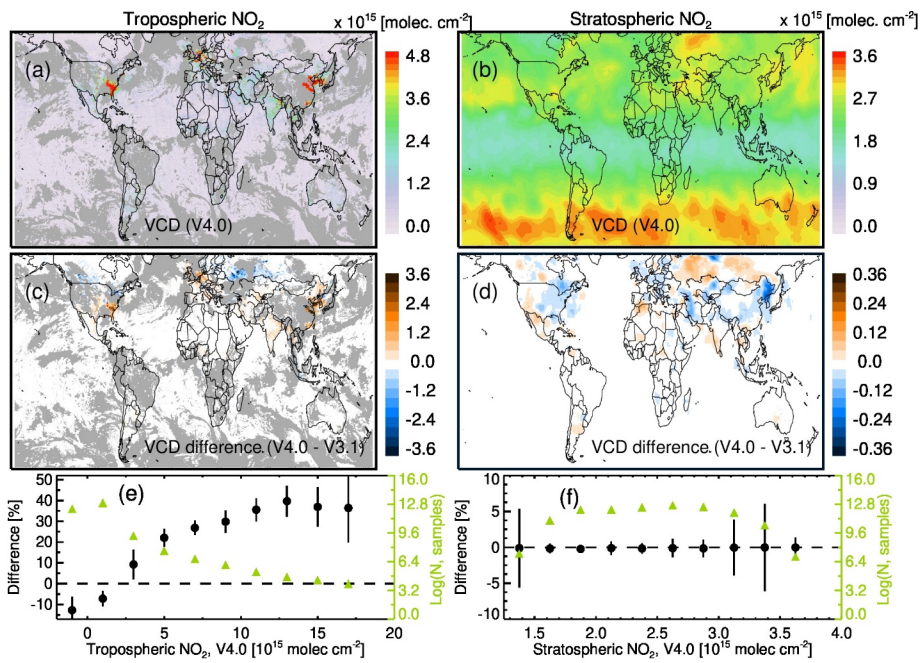
1369



1370

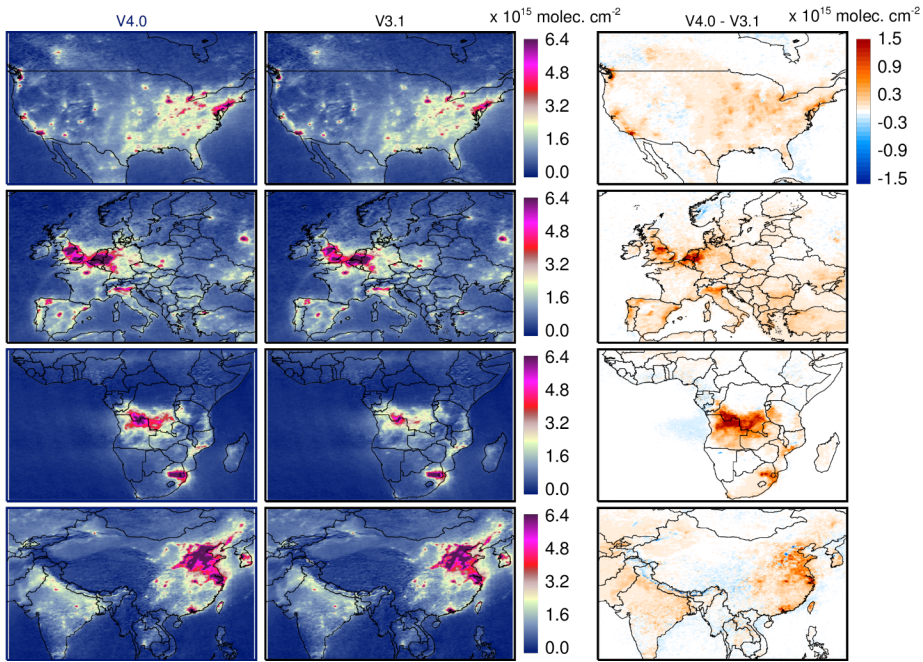
1371 **Figure 7:** The time series of OMI NO₂ SCD normalized by the geometric AMF for clear-sky and
 1372 partially cloudy conditions (CRF<0.5) over the Pacific Ocean. The data are separated by cross-
 1373 track scan position, comparing the presumably RA-free row 20 (black) with rows 44 (red), 45
 1374 (orange), and 46 (green). The row numbers are 0-based.

1375



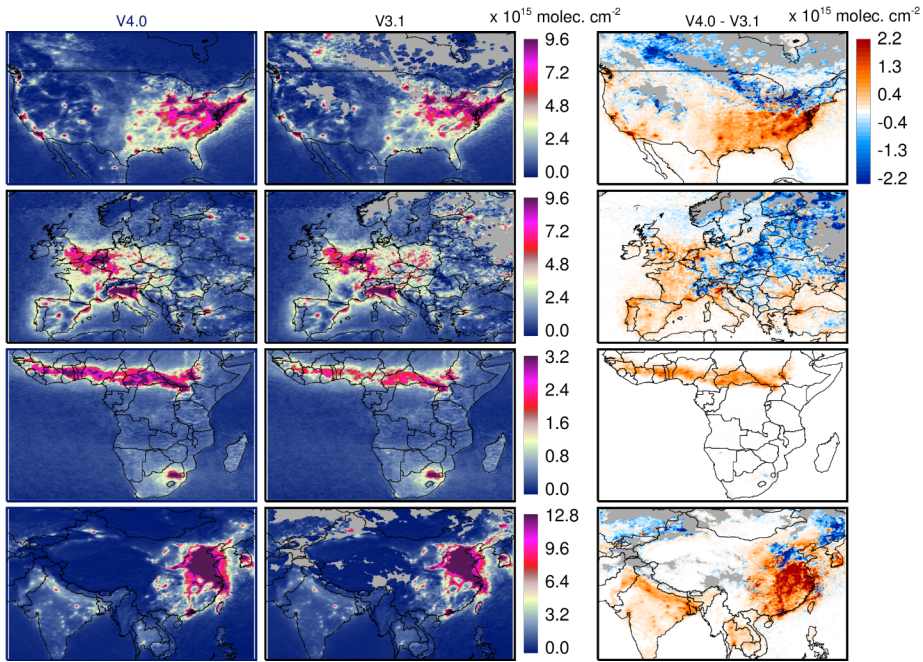
1376

1377 **Figure 8:** Tropospheric (a) and stratospheric (b) NO₂ VCD from V4.0 and their differences (c, d)
 1378 with V3.1 data (V4.0 – V3.1) for March 20, 2005. The gray color in the tropospheric NO₂ maps
 1379 represent cloudy areas (CRF>0.5). Bottom panels show average (black circles) and standard error
 1380 (vertical bars) of the relative difference, $100 \times (V4.0 - V3.1)/V3.1$, for tropospheric (e) and
 1381 stratospheric (f) NO₂ VCDs plotted as a function of respective NO₂ column amounts. The green
 1382 symbols represent the logarithm of the number of samples.



1383

1384 **Figure 9:** Three-month (June, July, August) average tropospheric NO₂ columns for low cloud
 1385 conditions (CRF<0.5) in 2005 over North America (1st row), Europe (2nd row), southern Africa
 1386 (3rd row), and Asia (4th row) from V4.0 (1st column), V3.1 (2nd column), and their difference (V4.0
 1387 – V3.1).



1388

1389 **Figure 10:** Same as Figure 9, but for December, January, and February. The gray areas represent
 1390 a lack of good observations as determined by data quality flags.

1391

1392

1393

1394

1395

1396

1397

1398

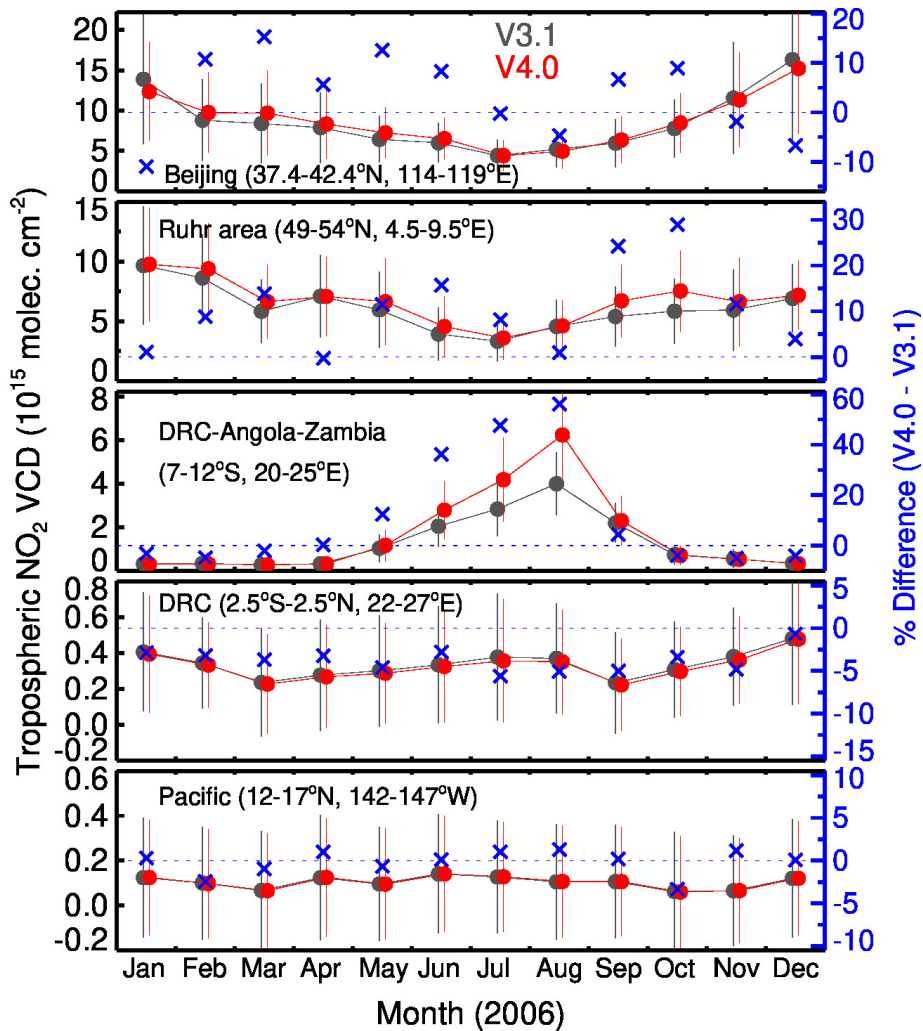
1399

1400

1401

1402

1403



1404

1405

1406

1407

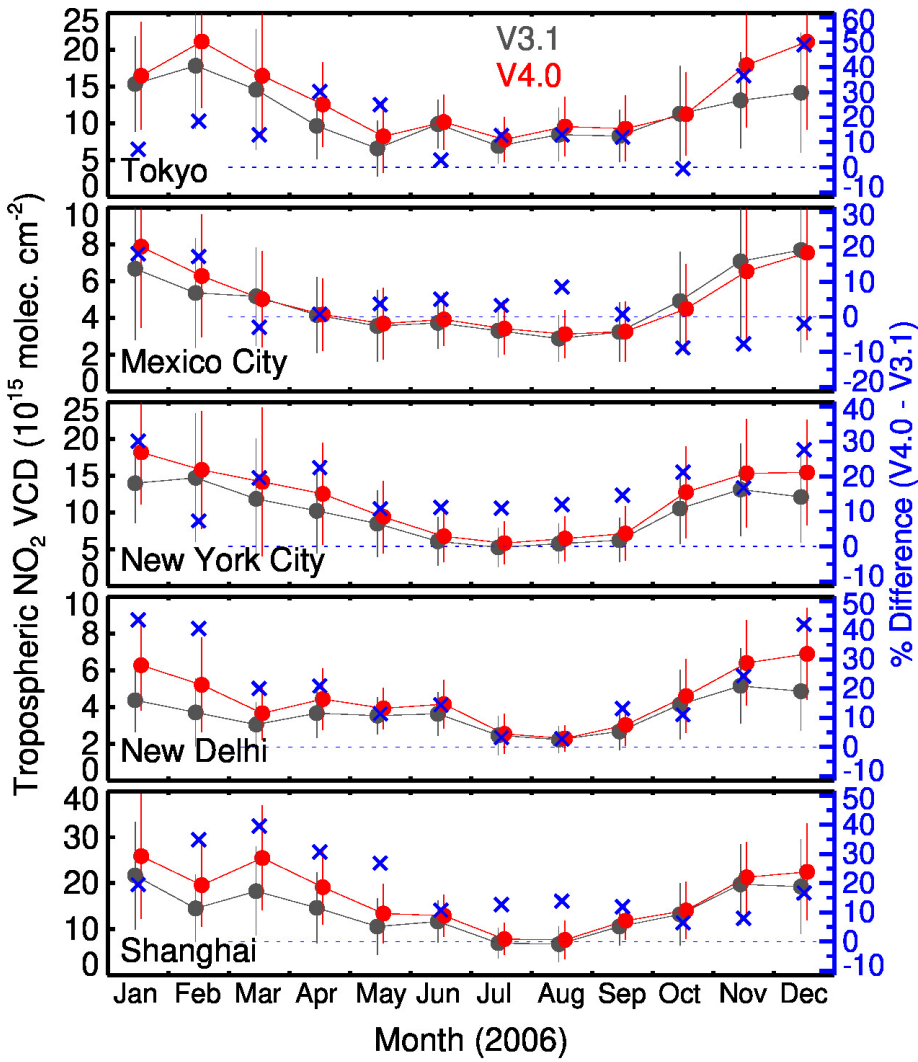
1408

1409

Figure 11: Monthly average tropospheric NO₂ columns in 2006 calculated from V3.1 (black) and V4.0 (red) data over selected 5° latitude × 5° longitude boxes from locations that are dominated by either anthropogenic (Beijing, China and Ruhr area, Germany), biomass burning (Democratic Republic of Congo (DRC), Angola, and Zambia), lightning (DRC), or no significant (Pacific) NO_x sources. The vertical bars show the monthly standard deviation. The blue symbols

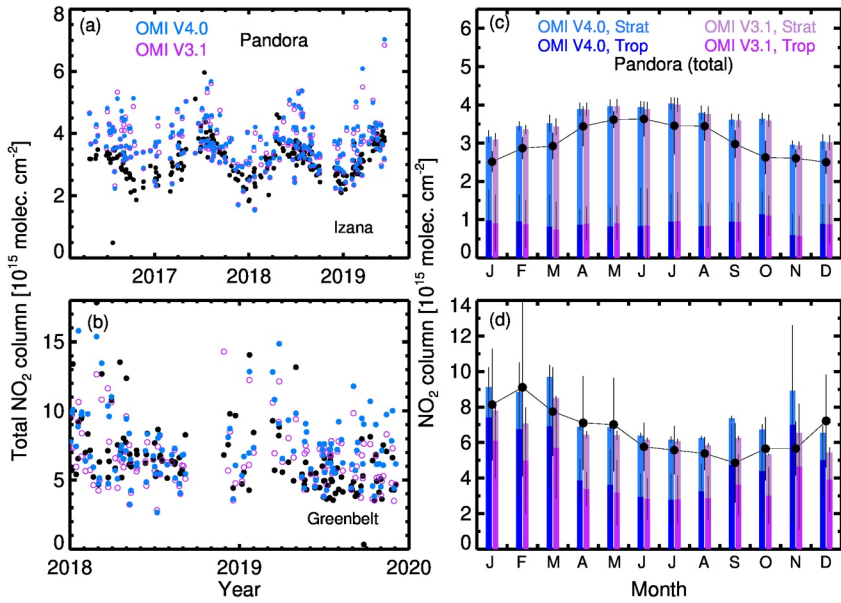
Formatted: Subscript

1410 that correspond to the right y-axis show monthly relative difference (in percent) between V4.0
 1411 and V3.1.



1412
 1413 **Figure 12:** Same as Figure 11, but for 1° latitude × 1° longitude wide box over the five highly
 1414 populated and polluted cities.
 1415

1416
1417

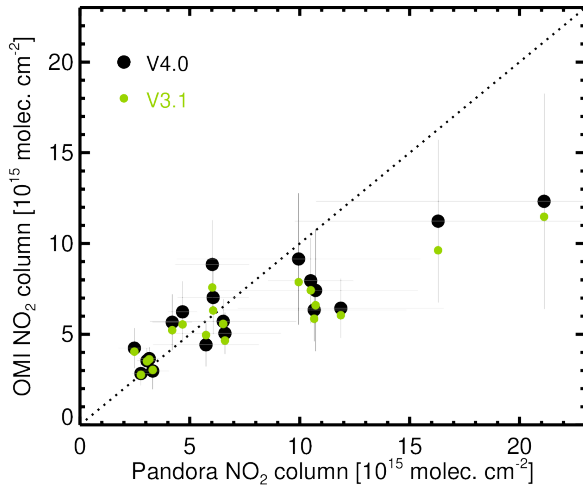


1418

1419 **Figure 13:** The time series of NO₂ total columns retrieved from Pandora (black circles) and OMI
1420 at (a) Izaña, Spain and (b) Greenbelt, Maryland, USA, with the OMI retrievals represented by the
1421 filled blue (V4.0) and open purple (V3.1) circles. Right panels show monthly variation of NO₂
1422 total columns at (c) Izaña for 2016–2019 and (d) Greenbelt for 2018–2019, as calculated from
1423 Pandora (black line with filled circles) and OMI measurements (bars). OMI NO₂ total columns

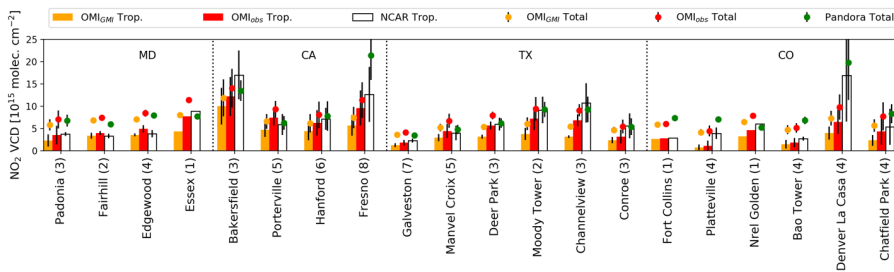
Deleted: 1

1425 retrieved with V4.0 (blue) and V3.1 (purple) are separated into tropospheric and stratospheric
 1426 components. The vertical lines represent the standard deviation from the average.
 1427



1428
 1429 **Figure 14:** The scatter plot of Pandora versus OMI V4.0 (black) and V3.1 (green) average total
 1430 column NO₂ for 18 Pandora sites. The vertical and horizontal lines represent the standard
 1431 deviations for Pandora and OMI, respectively. The dotted line represents the 1:1 relationship.
 1432

Deleted: 2



1433
 1434 **Figure 15:** Site average total (circles) and tropospheric (bars) NO₂ column data from P-3B spiral
 1435 (white bars), Pandora (green circles), and OMI (orange and red). The OMI tropospheric columns

Deleted: 3

1438 are derived using GMI-simulated (OMI_{GMI} , orange) and P-3B (OMI_{obs} , red) NO_2 profiles. The
 1439 vertical bars for sites with over 2 observations represent the standard deviations.

1440

1441 **Table 1.** Summary of algorithms and approaches used in the NASA NO_2 algorithms versions 3.1 and 4.0

Algorithm Component		Version 3.1 (Released 2018)	Version 4.0 (Released 2019)
Spectral fit	NO_2	Modified DOAS fit (Marchenko et al, 2015)	Same as in V3.1
	O_2-O_2	DOAS fit from KNMI (Veeffkind et al, 2016)	Modified DOAS fit (Vasilkov et al, 2018)
AMF	Terrain reflectivity	Monthly climatology (Kleipool et al., 2008)	Daily GLER data (Vasilkov et al., 2017; Qin et al., 2019; Fasnacht et al., 2019)
	Terrain pressure	At pixel center (calculated from terrain height and GMI terrain pressure)	Average over pixel (calculated from terrain height and GMI terrain pressure)
	Cloud pressure and fraction	Operational O_2-O_2 cloud product (OMCLDO2) v2.0 (Veeffkind et al., 2016)	New O_2-O_2 cloud product (OMCDO2N) derived using the GLER product (Vasilkov et al., 2018)
	Cloud radiance fraction	Calculated at 440 nm from OMCLDO2 v2.0 cloud fraction using VLIDORT-based look-up-table	Calculated at 440 nm from OMCDO2N cloud fraction using VLIDORT-based look-up-table
	Scattering weights	TOMRAD-based look-up table	Same as in V3.1
	A-priori NO_2 profiles	GMI-derived yearly varying monthly mean profiles at $1^\circ \times 1.25^\circ$	Same as in V3.1
Stripe correction		Based on data from $30^\circ S$ - $5^\circ N$ of 5 orbits	Same as in V3.1
Stratosphere-troposphere separation		Spatial filtering and interpolation (Bucsela et al., 2013), but with minor changes in box sizes	Same as in V3.1

1442

1443

1444

1445

1446

1447 **Table 2:** Comparison of OMI NO₂ retrievals based on a priori NO₂ profiles from GMI (OMI
 1448 V4.0) and P-3B aircraft observations (OMI_{obs}) with P-3B and Pandora column observations
 1449 during the DISCOVER-AQ field campaign. Shown here are correlation coefficient (r) and mean
 1450 difference, which is calculated as OMI minus validation data.

Campaign locations	OMI V4.0 vs P-3B		OMI _{obs} vs P-3B		OMI (V4.0) vs Pandora		OMI _{obs} vs Pandora	
	Mean diff. (%)	r	Mean diff. (%)	r	Mean diff. (%)	r	Mean diff. (%)	r
Maryland	-33.9	0.40	-5.0	0.69	-13.0	0.13	25.6	0.27
California	-44.6	0.81	-18.7	0.83	-49.8	0.33	-24.6	0.49
Texas	-53.7	0.68	-18.8	0.85	-25.3	0.67	31.7	0.81
Colorado	-66.2	0.70	-45.4	0.70	-67.6	0.70	-46.7	0.65
All	-50.3	0.74	-23.1	0.79	-46.9	0.56	-16.3	0.63

1451
 1452